

Morphology of the Virgo Cluster: Gas versus Galaxies

S. Schindler^{1,2,3,*}, B. Binggeli⁴, H. Böhringer²

¹ Astrophysics Research Institute, Liverpool John Moores University, Twelve Quays House, Egerton Wharf, Birkenhead L41 1LD, UK

² Max-Planck-Institut für extraterrestrische Physik, Giessenbachstraße, D-85478 Garching, Germany

³ Max-Planck-Institut für Astrophysik, Karl-Schwarzschild-Straße 1, D-85478 Garching, Germany

⁴ Astronomisches Institut der Universität Basel, Venusstrasse 7, CH-4102 Binningen, Switzerland

[the date of receipt and acceptance should be inserted later]

Abstract. We draw a quantitative comparison of the distribution of the galaxies and the intra-cluster gas in the Virgo cluster by extending the morphological analysis by Binggeli et al. (1987) to the intra-cluster gas. We use the Virgo Cluster Catalog in combination with data from the ROSAT All-Sky Survey. The galaxy distribution and the gas distribution are relatively similar. The steep density gradient southwest of M87 previously observed in the optical is also seen in the X-ray emission. In both wavebands the irregular structure of Virgo can be decomposed into three major subclusters centred on M87, M49, and M86. A new statistical method of subcluster decomposition is applied. Radial galaxy and X-ray density profiles of the three subclusters are fitted with β -models, allowing analytic deprojection. Comparison of these profiles reveals no significant difference between the galaxy number density and the smoothed galaxy luminosity density if the inner part is excluded ($r < 60'$, dominated by the central giant galaxy), i.e. there is no general luminosity segregation in the cluster. The gas density profile is steeper than the galaxy density profile in the inner part (again excluding the central galaxy), while this trend is reversed in the outer part. The turning point is around 300 kpc. A comparison among the subclusters shows the poorer the subcluster the steeper its radial profile, i.e. the more compact it is, both in the optical and the X-rays. This is in general agreement with recent N-body simulations by Navarro et al. (1997). The subcluster profiles for different Hubble types confirm the well-known result that the distribution of the late-type galaxies is more extended than the early types. Differential and integrated mass density profiles of the different components in the M87 and M49 subclusters are presented. The total, gravitating mass (dominated by dark matter) is inferred from the distribution of the X-ray gas assuming hydrostatic equilibrium. In the M87 subclus-

ter the gas mass is about three times the mass in galaxies (assuming a constant $M/L = 20$ for the single galaxies), while it accounts only for 8% to 14% of the total mass at 0.4 and 1 Mpc, respectively. In the M49 subcluster there is more mass in the galaxies than in the gas and the gas-to-total mass fraction is only 1%, which is unusually low for a cluster. The profiles of the projected mass-to-light ratio show relatively constant values around $500 M_{\odot}/L_{\odot,B}$.

Key words: Galaxies: clusters: individual: Virgo cluster - inter-galactic medium - dark matter - X-rays: galaxies

1. Introduction

Clusters of galaxies are the largest gravitationally bound aggregates of matter in the universe, being a mixture of dark matter (up to 90% of the total gravitating mass), hot gas (up to 30%), and galaxies (a few % of the total; for a recent review on clusters, see Böhringer 1995). Although clusters represent the highest peaks in the large-scale density field, most of them (even very rich ones) show significant substructure and therefore cannot be dynamically relaxed. This is usually taken as evidence that cluster formation is a prolonged process, or has set in only recently (say, around $z = 1$). Clearly, the study of substructure in clusters of galaxies should provide important constraints on structure formation in the universe in general.

Traditional studies of substructure rely on various statistical tests applied to the (projected) spatial and velocity distribution of (suspected) member galaxies (e.g., Fitchett 1988; West 1994; Girardi et al. 1997 and references therein). Since the advent of X-ray satellites, and in particular ROSAT (Trümper 1993), cluster substructure is also observed and mapped in the intra-cluster gas (e.g., McMillan et al. 1989; Briel et al. 1991, 1992; White et al. 1993).

* e-mail: sas@staru1.livjm.ac.uk

As both the galaxies and the hot gas are sitting in a common dark-matter potential, it is expected that both components show, to first order, the same distribution – which indeed is observed. However, there is also an important difference: the gas is dissipative, while the galaxies are (essentially) collisionless. In the case of subcluster merging, this can lead to significant deviations in the X-ray versus optical structure of a cluster (Schindler & Müller 1993), evidence for which is reported, e.g., for Abell 754 (Zabludoff & Zaritsky 1995) and Abell 2255 (Burns et al. 1995). The systematic comparison of the distribution of the X-ray gas and the cluster galaxies can therefore be regarded as a powerful tool to assess the dynamical state of a cluster.

In this paper we present such a comparison of gas versus galaxies for the Virgo cluster of galaxies. The Virgo cluster is the nearest, fairly rich galaxy cluster where such a study can also be carried out with greatest detail. In spite (or rather because) of its proximity, this cluster has been difficult to map, simply because of its large angular extent in the sky (roughly 100 deg^2). For a complete, deep, high-resolution optical study it had to await the Las Campanas Survey, which resulted in the Virgo Cluster Catalog (VCC, Binggeli et al. 1985). Likewise, following a first large-scale scan with GINGA (Takano et al. 1989), it took the ROSAT All-Sky Survey (Voges et al. 1996) to cover the cluster completely with good resolution in the X-ray waveband.

Based on the VCC and supplementary kinematic data, Binggeli et al. (1987, hereafter BTS87; 1993) studied the spatial and velocity distribution of different morphological types in the Virgo cluster. Confirming in part earlier results by de Vaucouleurs and others (cf. BTS87), three major subclusters centred on the giant ellipticals M87, M86, and M49 were identified. In a subsequent study of the X-ray structure of Virgo based on ROSAT All-Sky Survey data by Böhringer et al. (1994) these three subclusters became evident by their extended X-ray halos. Böhringer et al. (1994) also provided a first global comparison of the gas versus galaxy distribution and found additional evidence for the imminent or ongoing merging of the M87 and M86 subclusters. The Virgo cluster is a typical irregular cluster that appears to be still in the making (see also Binggeli, 1998, for a general review).

Here we combine the VCC and ROSAT All-Sky Survey data bases to construct and intercompare the 3D-radial profiles in galaxy number density, luminosity density, gas density, and mass density for all three major subclumps of the Virgo cluster.

The rest of the paper is organized as follows. After a brief description of the data sources (Sect. 2), we present a purely qualitative and global comparison of the optical versus X-ray structure of the Virgo cluster, addressing also the differences with respect to morphological type (Sect. 3). Starting with Sect. 4 we concentrate on the three subclusters around M87, M86, and M49 and describe a

new method of how to decompose the cluster into subclusters. A detailed, quantitative comparison for the radial profiles of the three subclusters, based in large part on β -profile fitting, is then given in Sect. 5. Mass density and mass-to-light ratio profiles are presented in Sect. 6. Finally, Sect. 7 gives our summary and conclusions.

A mean Virgo cluster distance of 20 Mpc, corresponding to a true distance modulus of $(m - M) = 31.5$ (cf., e.g., Tammann & Federspiel 1996), is assumed throughout this paper.

2. Data

For the optical part of this study we use the positions, types and total blue (B) magnitudes of the 1292 member galaxies listed in the VCC (Binggeli et al. 1985, membership as updated in Binggeli et al. 1993). This catalog was compiled from the Las Campanas Survey of the Virgo cluster, covering an area of $\approx 140 \text{ deg}^2$. The VCC is complete to an apparent magnitude $B = 18$ (corresponding to $M_{B_T} = -13.5$ with the adopted distance of 20 Mpc) and contains in addition many fainter dwarf galaxy members down to $B = 20$. For 403 of the galaxies radial velocity information is also available. These velocities were crucial for the identification of the M86 subclump (Binggeli et al. 1993). The cluster membership of a galaxy was reckoned essentially from its morphological appearance, guided by the available velocity data. It has recently been confirmed by Drinkwater et al. (1996) that the morphological membership selections are generally correct.

For transforming observed galaxy magnitudes into true luminosities we assume an extinction value for galactic absorption of 0.15 mag, which is an average value for all Virgo galaxies from the RC3 (Schröder 1995). To get a rough estimate of the mass of a galaxy (Sect. 6) we employ a B-band mass-to-light-ratio of 20, independent of the Hubble type. The faintest galaxies in the VCC have apparent B magnitudes of 20, while the most luminous Virgo galaxy, M49, has $B = 9.31$ mag. This gives almost a factor of 20000 in luminosity or mass between these extreme galaxies.

The distribution of the hot intra-cluster gas is inferred from the X-ray brightness distribution as mapped by the ROSAT All-Sky-Survey (Voges et al. 1996). The Virgo area was scanned from November 1990 to January 1991 with an average exposure time of about 450 seconds and a spatial resolution of 20 - 60". Here we use the X-ray emission detected in the ROSAT hard band (channel 52 to 201 corresponding roughly to the energy range 0.5-2.0 keV).

For constructing the X-ray radial profiles of the three subclusters (Sect. 5), 13 point sources had to be excluded. Most of these background (QSO or distant cluster) or foreground (stellar) sources are identified in Fig. 1 of Böhringer et al. (1994). For the analysis of the M87 subcluster, the regions around M49 and M86 had additionally

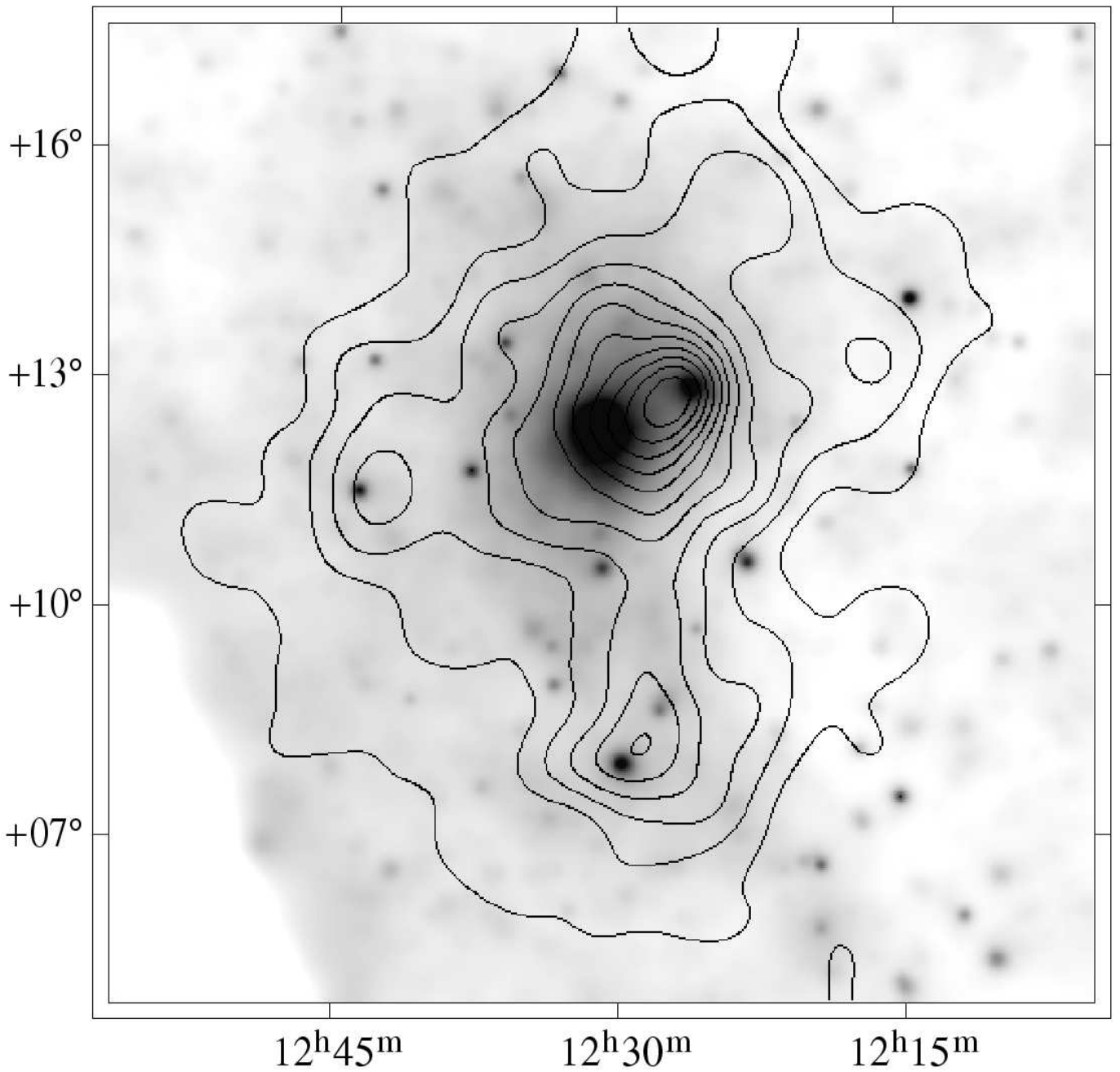


Fig. 1. Comparison of the X-ray and the optical appearance of the Virgo cluster. The greyscale image shows, in a logarithmic scale, the X-ray emission as observed by the ROSAT All-Sky Survey in the hard band (0.5 - 2.0 keV) (Böhringer et al. 1994, where also most of the point sources are identified). It is smoothed with a Gaussian filter with $\sigma = 24'$ on the faintest levels and decreasing filter size with increasing surface brightness. The contours show the number density of the 1292 member galaxies of the VCC smoothed again with a Gaussian of $\sigma = 24'$. The spacing of the contours is linear. The lowest contour line and the contour spacing is 1.5×10^{-3} galaxies per \square' . The image has a size of $12.8^\circ \times 12.8^\circ$. North is up and West to the right. The dominant dark blob is centred on M87 ($\alpha_{2000} \approx 12^{\text{h}}30^{\text{m}}$, $\delta_{2000} \approx 12^\circ 23'$). For the identification of further galaxies, cf. Fig. 2.

to be excluded. For the analysis of the M49 subcluster, two different approaches were used which give insignificantly different results: (1) Excluding a rectangular region north of the M49 halo and (2) excluding a sector in the north with an angle of 120° .

3. A qualitative optical and X-ray comparison of the Virgo cluster

Fig. 1 is a superposition of the X-ray emission in the Virgo cluster region measured by ROSAT (greyscale image) and the optical distribution of VCC member galaxies (number density contours). Both distributions are smoothed with a Gaussian filter with $\sigma = 24'$. For a direct plot of all VCC members, giving an impression of how the Virgo cluster appears in the sky, the reader is referred to BTS87. For easy identification of the major cluster members and the substructures associated with them, we have repeated the contour image for all member galaxies in Fig. 2a, where these galaxies are plotted with different symbols. The X-ray image is repeated in Fig. 2 as well (Fig. 2e), this time in logarithmic contours, to guide the optical versus X-ray comparison. The smoothing scale of $24'$ is arbitrary but has been optimized to avoid the noise of single galaxies by too little smoothing on the one hand, and the smearing out of substructure by too much smoothing on the other.

Already at a glance the Virgo cluster appears as a complex system. There is a pronounced double structure in the direction N-S. The Northern clump, called “cluster A” in BTS87, is dominated by M87, which coincides with the maximum of the X-ray emission in the whole area (the large dark blob in the centre of Fig. 1). The Southern, much less pronounced clump, called “cluster B” in BTS87, coincides with M49, another supergiant elliptical that is even slightly brighter than M87. However, as emphasized in BTS87, the galaxy density contours do not peak on M87 but almost 1° WNW of it – more than halfway in the direction to M86, which is yet another giant E galaxy (see Fig. 2a; in Fig. 1 M86 is the second-ranked dark spot). The reason of this “mispointing” of M87 is now clear: the Northern clump itself is a double system comprising the dominating, massive subcluster centred on M87 and a smaller subcluster centred on M86. This view is supported by the existence of a swarm of low-velocity dwarf galaxies around M86 (which itself has a negative velocity, Binggeli et al. 1993) and the extended X-ray halo of M86 (Böhringer et al. 1994). The M86 subcluster seems to fall into the M87 subcluster from behind (see also Binggeli 1998), bringing the previous picture of a single galaxy being stripped by the intra-cluster medium of the Virgo cluster (Forman et al. 1979; Rangarajan et al. 1995) in disfavour.

We thus deal essentially with three major subclumps, or subclusters (as they will henceforth be called): centred on the giant ellipticals M87, M86, and M49. They are

readily visible as dark spots in Fig. 1. Note that these X-ray sources are not point sources but are extended: the hot gas is sitting in the potential of the (extended) subclusters.

Clearly there is more, but rather spurious substructure in the Virgo cluster: in particular there is a lump in the East around the S0 galaxy M60, another one around the well-known spiral M100 in the North and a third one WNW of M86 (see Fig. 2a). Overall, the irregular, asymmetric structure of Virgo can be described by two distinct axes: one stretching N-S from M100-M87/86-M49, and one E-NW from M60-M87-M86. Remarkably, the latter axis is perfectly aligned with the jet of M87 (cf. Binggeli 1998).

We emphasize that no depth effects are considered here. There is weak evidence that the southern M49 subcluster is slightly more distant than the northern M87 subcluster (Federspiel et al. 1998), but the effect is not significant. On the other hand, Tonry et al. (1990) and Morris & Shanks (1998) claim that M49 itself is lying considerably in the foreground. However, this claim is based on the “surface brightness fluctuations” method for elliptical galaxies whose reliability is still debated (for a detailed discussion of the distance and the depth of the Virgo cluster see Binggeli 1998). Hence it seems safe at present to assume that, to first approximation, all Virgo subclusters and their central beasts are at the same distance.

3.1. Hubble type dependence

The number density distribution for the various galaxy types in the Virgo cluster is shown in Fig. 2b (early-type dwarfs, i.e. dE and dS0), 2c (early-type giants, i.e. E and S0), and 2d (late types, i.e. spirals and irregulars). Confirming the results of BTS87 we find very different distributions for the different types. The dwarf ellipticals (Fig. 2b) have a distribution very similar to that of all galaxies (Fig. 2a), simply because they make up $3/4$ of the total cluster population. The ellipticals and S0s (Fig. 2c) show a less extended distribution and are more concentrated to the subcluster centres, i.e. the X-ray maxima (compare with Fig. 2e). In sharp contrast, the distribution of the spirals and irregulars (Fig. 2d) is very extended and shows no correlation with the X-ray emission. Note also the difference in the type-mix between the various clumps. The M49 subcluster is obviously spiral-rich.

All of these trends, which of course reflect the general morphology-density relation (Dressler 1980), appear even more pronounced in the luminosity-weighted distributions shown in Fig. 3. The luminosity distributions are obviously dominated by the light peaks of single bright galaxies, especially (not surprisingly) of M87, M86, M49, and M60 (most pronounced in Fig. 3c). The compact, spherical contours around these galaxies, also around bright spirals in Fig. 3d, merely reflect the smoothing scale (Gaussian σ) of $24'$. The galaxies themselves are much smaller. When M87, M86, M49, and M60 are subtracted, the luminosity distribution changes drastically (Fig. 3e, to be compared

with 3a). There remains an extended region of enhanced galaxy density in the M87/M86 region, however, while the luminosity density around the position of M49 becomes very low, i.e. the optical luminosity of the M49 subcluster is very strongly dominated by M49 itself.

There is no way to obtain a smooth luminosity distribution when the galaxies span a factor of 20 000 in luminosity. This problem will be encountered again below.

4. A new method for subcluster decomposition

As the Virgo cluster is not a relaxed, symmetric system but consists of several subclusters (cf. above), it is impossible to treat it as a single entity with spherical symmetry. Each subcluster has to be analysed separately. The next task, then, is to decompose the cluster cleanly into the subclusters identified around M87, M86, and M49. Two methods to achieve this have been employed here, each resulting in an independent data set.

In the first, more conventional method one simply excludes certain regions around the other subclusters. To construct a radial profile of the M87 subcluster we have excluded a rectangular area of $(70\text{arcmin})^2$ around M86, and of $(150\text{arcmin})^2$ around M49. The same procedure can also be used for the X-ray profile. For profiles centred on M49 we have excluded all data north of a horizontal line at a distance of 112'5 from M49. Extracting a profile of the M86 subcluster, however, is very difficult because it is so close to, and much smaller and less luminous than, the M87 subcluster. Contamination by the M87 subcluster is unavoidable. Nevertheless, we have made an attempt to determine a profile of the M86 subcluster by simply subtracting the contribution of the M87 subcluster (see Sect. 5). In the following we call all of these profiles constructed by excluding certain regions *R-profiles*.

Contaminations from the outer regions of the neighbouring subclusters are of course a principal shortcoming of the *R*-method. To overcome this difficulty and to test how large the uncertainties in the profiles are, we have developed a new method of cluster decomposition. In this method, each galaxy is assigned to be member of that subcluster to which it most probably belongs.

Figure 4 shows schematically how the method works. Suppose the spatial distribution of each subcluster is known and is taken directly as probability distribution. The position of a particular galaxy within the cluster then determines the probability for this galaxy to belong to either subcluster: P_s (M87), P_s (M49) and P_s (M86). For simplicity we show only one spatial dimension in Fig. 4, but of course we use the full two-dimensional information for the subcluster assignment. As for all galaxies except the dwarfs velocity information is available in addition, we apply the same procedure for (one-dimensional) velocity space, resulting in another probability P_v . The final membership probability for a galaxy is then simply the product

$P = P_s \times P_v$, assuming that P_s and P_v are statistically independent. Finally, a galaxy is assigned to that subcluster to which it has the highest probability to belong.

To model the spatial distribution of the subclusters we have used spherically symmetric β -models (see Sect. 5.1 below) with different core radii for the different subclusters and for different Hubble types. The core radii (for $\beta = 1$) were taken from BTS87 or, where not available, estimated from data given in BTS87 and Binggeli et al. (1993). The model profiles were centred on the three giant galaxies. Galaxy types were sorted into three groups (as above in Figs. 2 and 3): E+S0, dE+dS0, and Sp+Irr, with 85, 963 and 244 galaxies, respectively. The velocity distributions were modeled by Gaussians, centred on the velocities of the central galaxies (M87: $v = 1258 \text{ km s}^{-1}$, M49: $v = 969 \text{ km s}^{-1}$, M86: $v = -227 \text{ km s}^{-1}$) and with different velocity dispersions for different subclusters and different Hubble types, as given in Binggeli et al. (1993), or as reckoned for the M86 subcluster from data therein.

All core radii and velocity dispersions adopted are listed in Table 1. The distributions were normalized to the total numbers of galaxies for the subcluster listed in the bottom line of Table 1. From these numbers we see that the M87 subcluster comprises roughly three times as many galaxies as the M49 subcluster, which in turn is about six times the M86 subcluster. These ratios are of course different in terms of luminosity or mass (cf. below).

The final results are not very sensitive to the exact choice of the input parameters. This becomes evident e.g. in the β -value: although for subcluster decomposition always $\beta = 1$ was used, there is a large spread in the β -values in the final results.

Table 1. Input parameters for the membership assignments. The first block shows the core radii in kpc for the various subclusters and Hubble types. The second block lists the velocity dispersions in km s^{-1} . The last line gives the total number of galaxies in each subcluster.

		M87	M49	M86
r_c	E+S0	420	420	260
	dE+dS0	570	570	340
	Sp+Irr	1220	1220	680
σ	E+S0	670	320	120
	dE+dS0	720	370	120
	Sp+Irr	850	580	120
number of galaxies		920	317	55

In the following all subcluster profiles constructed with this probability method are called *P-profiles*. In Fig. 5 we show the three subclusters, separately in three panels, as they result from assigning member galaxies by the new probability method. Clearly, this method has its drawbacks, too. As the velocities of the central galaxies M87

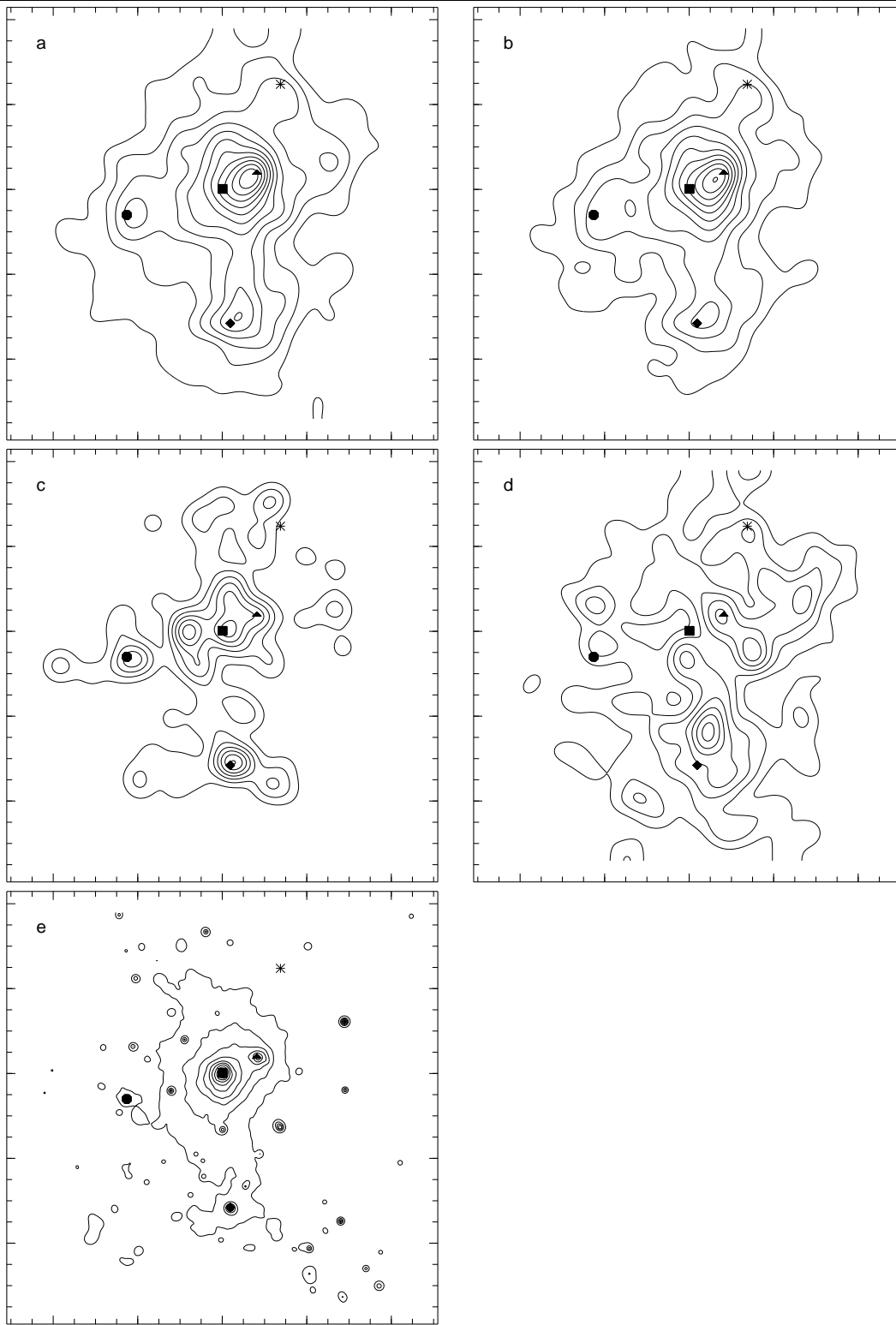


Fig. 2. Distributions of the different galaxy types. Number densities smoothed with a Gaussian of $\sigma = 24'$ are shown. (a) all galaxy types, (b) dwarf elliptical and dwarf S0 galaxies, (c) elliptical and S0 galaxies, (d) spiral and irregular galaxies. The contours are linear with spacings of (a) 1.5×10^{-3} galaxies/ \square' , (b) 1.3×10^{-3} galaxies/ \square' , (c) 2.2×10^{-4} galaxies/ \square' , (d) 3.6×10^{-4} galaxies/ \square' . The level of the first contour line is equal to the spacing. For better comparison with Fig. 1 the positions of five galaxies are marked: M87 (square), M49 (diamond), M86 (triangle), M60 (octagon), M100 (star). (a) is the same as the contours in Fig. 1. For comparison the X-ray image is shown again in (e) with logarithmically spaced contours. The size of each image is $12.8^\circ \times 12.8^\circ$. The distance between two tickmarks is $42'$.

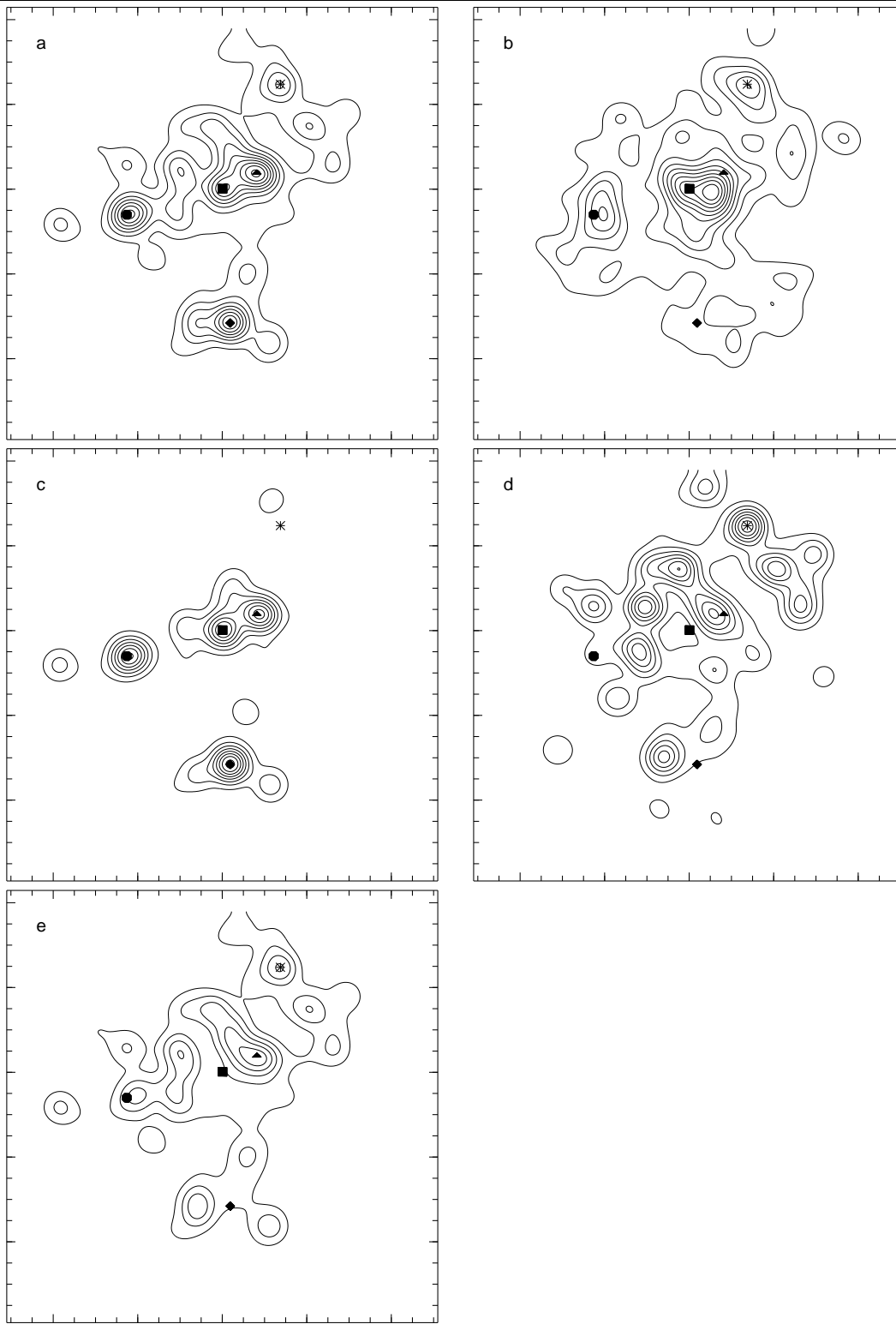


Fig. 3. Luminosity-weighted densities of the different galaxy types. (a) all galaxy types, (b) dwarf elliptical and dwarf S0 galaxies, (c) elliptical and S0 galaxies, (d) spiral and irregular galaxies, (e) all galaxies except for the four elliptical galaxies M87, M49, M86, and M60. The contours are linear with spacings of (a) $7.7 \times 10^6 \mathcal{L}_{\odot,B}/\square'$, (b) $4.5 \times 10^5 \mathcal{L}_{\odot,B}/\square'$, (c) $6.8 \times 10^6 \mathcal{L}_{\odot,B}/\square'$, (d) $3.6 \times 10^6 \mathcal{L}_{\odot,B}/\square'$ and (e) $7.7 \times 10^6 \mathcal{L}_{\odot,B}/\square'$. The level of the first contour line is equal to the spacing. Smoothing and symbols as in Fig.2.

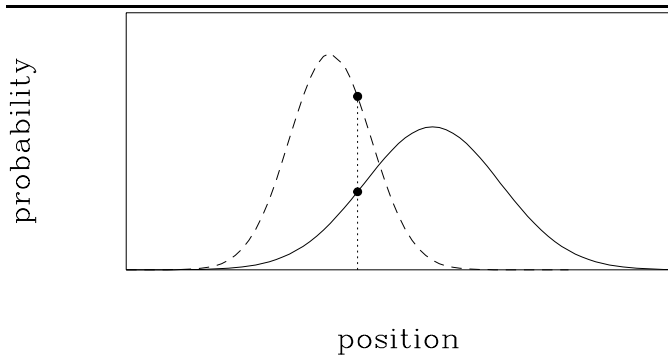


Fig. 4. Schematic diagram to illustrate the technique of subcluster assignment. The solid and the dashed lines show the probability distributions of two subclusters. A galaxy at the position of the dotted line would have a larger probability to belong to the dashed subcluster.

and M49 are very similar, and M86 is distinct by its negative velocity, the decomposition into the M87 and M86 subclusters rests mainly on the velocities, while the distinction between the M87 and the M49 subclusters is achieved mainly by the positional criterion. This is the reason why the outermost contours of the M87 and M49 subclusters are artificially flattened in the direction towards each other (Figs. 5a and b).

The three subclusters are distinctly different in their appearance. In accord with the relative galaxy populations mentioned above, the M87 subcluster is the largest and most extended one, the M49 subcluster is second, and the M86 subcluster is very small. What is more interesting: the smaller the subcluster the more compact it is, both in the number density distribution and the light distribution. In particular the M86 subcluster appears very compact. This trend is encountered again in the profile analysis below. We regard this as a principal result of the present paper.

The luminosity distributions of the three subclusters are shown in Figs. 5b, d and f. Again we see how these are dominated by single giant galaxies.

5. Quantitative optical – X-ray comparison of the Virgo cluster

5.1. How to compare optical galaxy densities with X-ray surface brightnesses

In different wavelengths different quantities are observed. In the optical one observes a galaxy density projected in the plane of the sky, while the X-ray emission measured is proportional to the projection of the *square* of the gas density. To make galaxy and gas densities comparable, one has to derive *spatial* densities by deprojecting the observed quantities. Fortunately, this is easily done with the β -model (Cavaliere & Fusco-Femiano 1976). The optical, projected galaxy density can be modeled by

$$n = n_0 \left(1 + \frac{r^2}{r_c^2} \right)^{-\frac{3}{2}\beta + \frac{1}{2}} \quad (1)$$

where r_c is the core radius, β is the slope parameter and n_0 is the central galaxy density. Likewise, the surface brightness distribution in X-rays can be modeled as

$$S = S_0 \left(1 + \frac{r^2}{r_c^2} \right)^{-3\beta + \frac{1}{2}} \quad (2)$$

with S_0 as central surface brightness. The resulting deprojected density for the optical galaxy distribution, as well as for the X-ray gas distribution is then

$$\rho = \rho_0 \left(1 + \frac{r^2}{r_c^2} \right)^{-\frac{3}{2}\beta} \quad (3)$$

with the central spatial density ρ_0 .

This means that we merely have to determine the best-fitting core radii r_c and slope parameters β for both the observed optical and X-ray profiles and we can for each derive a spatial density profile after Eq. (3) and then compare them. For convenience, the central spatial densities – galaxy number density, luminosity density, and gas density – will be normalized to 1 for all profiles.

Although the profile of Navarro et al. (1995, NFW profile) might be physically more meaningful, we do not use it here because it cannot be (de)projected in such an elegant way as the β -profile.

5.2. Construction of radial profiles: P-profiles and R-profiles

In the following we describe how the radial profiles of the subclusters were constructed. The resulting profiles are shown Fig. 6 – number density profiles in the left panels, luminosity density profiles in the right panels. The best-fitting β -model parameters associated with these profiles, also including Hubble-type-specific profiles to be discussed in the following subsections, are listed in Table 2 (number density) and Table 3 (luminosity density). It should be remembered that the central spatial density of the profiles is normalized to 1 throughout.

For the number density profiles we have grouped the galaxies into bins of equal numbers of galaxies, i.e. depending on the number of galaxies in the subset we have a different number of bins. This number is also listed in Table 2. The radius of the bin is defined as the mean value of all radii of the galaxies in the bin.

The luminosity profiles pose some difficulties (as noted already by BTS87). The huge differences between the luminosities of the faint and the bright galaxies result in a huge scatter in the profile because single bright galaxies contribute a major fraction to the luminosity of one bin.

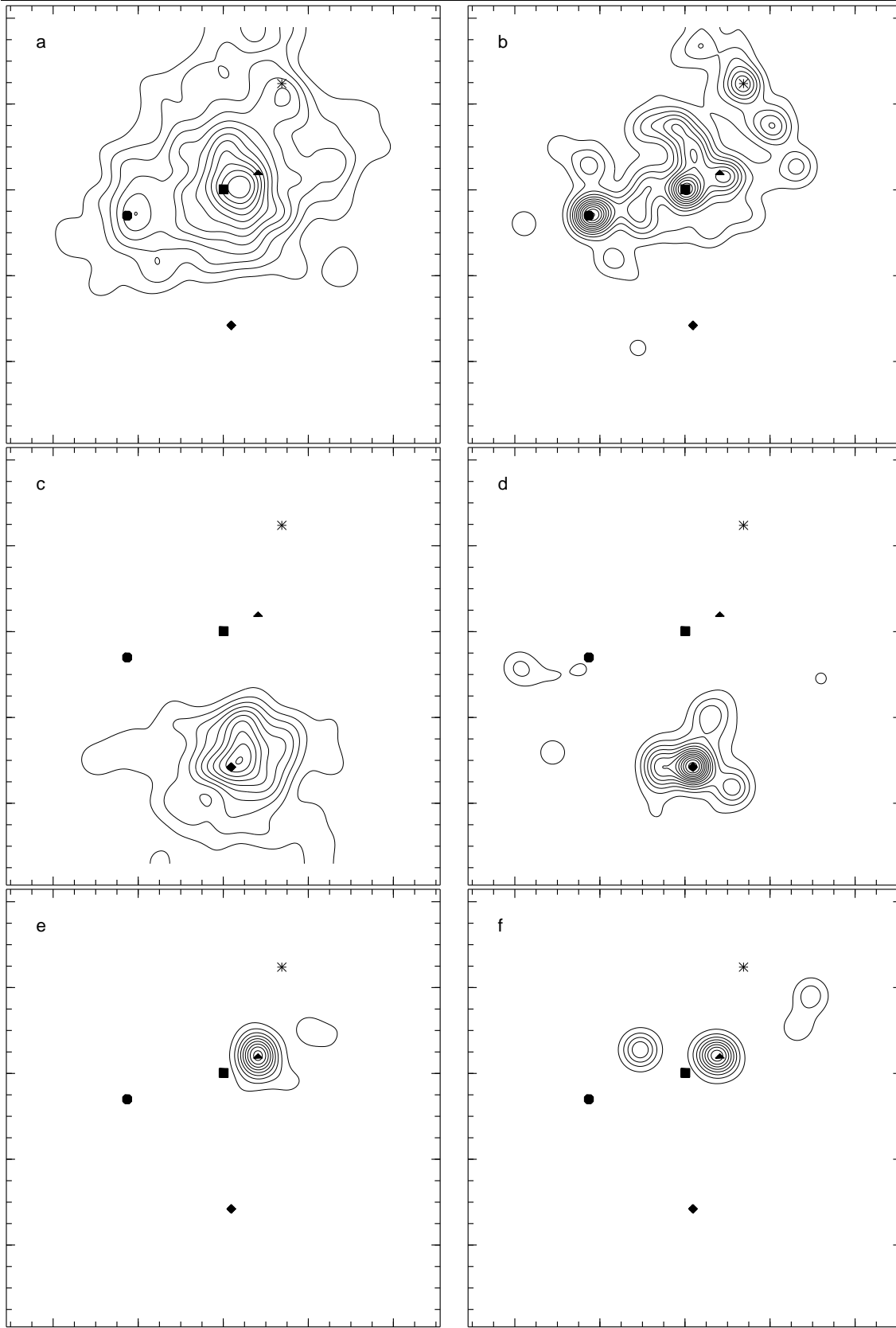


Fig. 5. Galaxy distribution in the subclusters separated by method *P*. Left panels: number densities, right panels: luminosity-weighted densities. (a) and (b): M87 subcluster, (c) and (d): M49 subcluster, (e) and (f) M86 subcluster. All distributions are smoothed with a Gaussian with $\sigma = 24'$. The contours are linear with spacings of 1.1×10^{-3} galaxies/ \square' in (a), 8.9×10^{-4} galaxies/ \square' in (c), 6.7×10^{-4} galaxies/ \square' in (e) and $4.5 \times 10^6 \mathcal{L}_{\odot, B}/\square'$ in (b), (d) and (f). The level of the first contour line is equal to the spacing. For better comparison with Fig. 1 the positions of five galaxies are marked: M87 (square), M49 (diamond), M86 (triangle), M60 (octagon), M100 (star). It is obvious that the subclusters are very different in size.

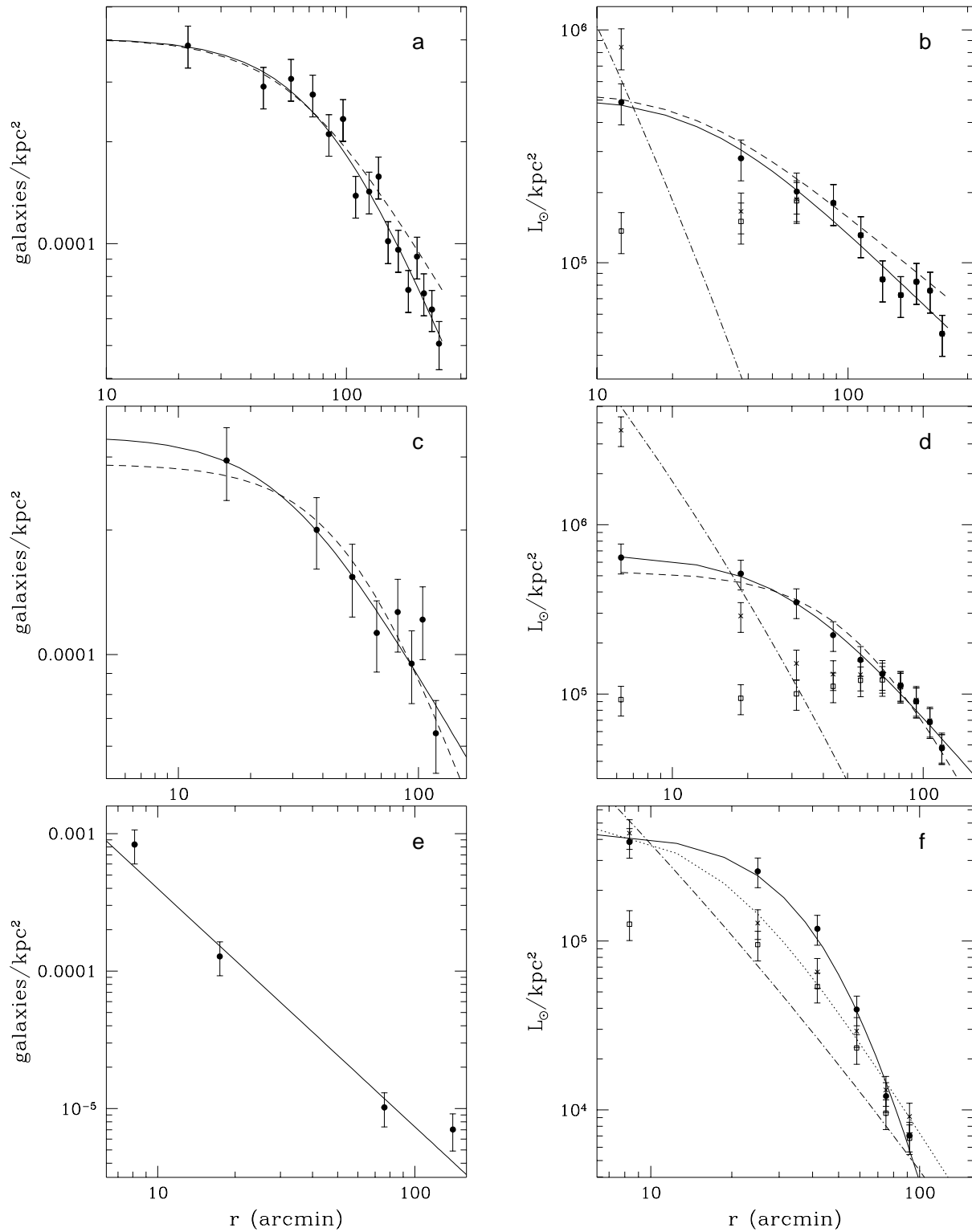


Fig. 6. Left panels: profiles of projected number density around M87 (a), M49(c), and M86(e) from P -selected galaxies (filled circles). The solid lines represent fits with β models. For comparison, the β -model fits to the corresponding R -profiles are shown as dashed lines. The right panels show projected luminosity densities around M87 (b), M49 (d), and M86 (f) from P -selected galaxies. The filled circles represent the P -profiles after applying the Gaussian smoothing described in the text. Solid and dashed lines are again best-fitting β -models to P and R -profiles, respectively. The profiles marked with crosses are the sum of the open squares and the true central galaxy profiles (dash-dotted lines) as observed by Caon et al. (1993). The only acceptable β -fit to the crosses for M86 is shown as dotted line in (f).

We tried to reduce the scatter by increasing the number of galaxies per bin. But even with 100 galaxies per bin the scatter remains large. Also binning the galaxies into bins with a minimum luminosity does not produce acceptable profiles. Fits to these profiles would almost give random results.

The only way to obtain acceptable luminosity profiles is to smooth first the galaxy distribution – as it is shown in Fig. 5 – and to construct the profiles subsequently from the smoothed image. A Gaussian of $\sigma = 24'$ proved to be large enough to obtain good fits. With smaller smoothing lengths the distribution is still dominated by single high-luminosity bins. With the smoothing applied first we could not do a binning by equal numbers of galaxies, instead we chose a constant bin size over the profile. For M87 and M49 we used 10 bins while for M86 we had to reduce the outer cut-off radius because of the strong contribution of M90, so we ended up with only 6 bins for this subcluster. The results of the fits do not depend on the bin size: tests with other bin sizes gave very similar results.

All profiles have an outer cut-off radius of $250'$ or less (see Table 2 and 3.), limited by the coverage of the VCC. The error bars shown in Fig. 6 have also been used for the fits (see Tables 2, 3 and 5). For the number densities, these are \sqrt{N} errors, where N is the number of galaxies per bin. For the luminosity profiles this number is not available because of the smoothing procedure applied before. As here 25 is an average number of galaxies per bin, we have assumed a corresponding error of 20% to determine χ^2 for the luminosity profile fits. A global change in the error of the data points would result in different errors of the fit parameters and a different χ^2 , but would not affect the fit parameters themselves.

In Fig. 6, binned profiles are only shown for P -selected subclusters. However, best-fitting β -models are plotted for both P and R -profiles (the luminosity density R -profile for the M86 subcluster, constructed by subtracting a smoothed image of the M87 subcluster, is very uncertain and is not shown in the figure). The comparison of P and R -profiles shows that in general they agree quite well, with a tendency of the P -profiles to be somewhat steeper. The flattening in the R -profiles is probably caused by contaminations from the outer (non-excluded) parts of the (nominally) excluded subclusters. The alternative explanation would be that the steeper slope of the M87 P -profile is due to the relatively strong gradient in direction to M49 at large radii (see the outer contours in Fig. 5a) which might leave a residual with the P -method. However, this second possibility was rejected by a test, in which the P -fits were repeated with a smaller cutoff radius of $170'$, finding no difference.

The principal caveat with the smoothed luminosity profiles is of course that in the inner part the profiles are entirely determined by the smoothed central giant galaxies. The core radii simply reflect the smoothing scale length. We have encountered this problem before in Sect. 3

in connection with Fig. 3. The effect is obvious also in Fig. 5 (right panels). To see the exact contribution of the central galaxies we have subtracted their light from the luminosity profiles and then smoothed the rest as before (open squares in Fig. 6, right panels). Removing these central giants renders the luminosity profiles crater-shaped, at least for the M87 and the M49 subclusters where the central galaxies are very massive and dominant. For the M86 subcluster the effect is less strong.

To get a true luminosity profile for the inner part of a subcluster, one has to involve the actual light profile of the central galaxy itself (assuming, as we do, that the subcluster is exactly centred on it). Surface brightness profiles, parametrized by the generalized de Vaucouleurs law $r^{1/n}$, are provided by Caon et al. (1993) for all three giants M87, M49, and M86. Their B -band luminosity profiles based on the Caon et al. data are shown as dash-dot lines in Fig. 6 (right panels). Clearly, and perhaps not surprisingly, the profiles of M87 and M49 are much steeper than the profiles of their embedding subclusters. It should be noted that the parametrized Caon et al. (1993) profiles are accurate enough for our purposes; they were also checked to reproduce the observed total luminosities when integrated.

These galaxy profiles can now be added to the decapitated subcluster luminosity profiles (i.e. the profiles constructed without central galaxies). The resulting “true” luminosity profiles are shown as crosses in Fig. 6. The profiles of the M87 and M49 subclusters are now no longer monotonic but have a local minimum (between $30'$ and $50'$) and a local maximum (between $60'$ and $70'$). The profile of the M86 subcluster remains monotonic because M86 itself is rather shallow. This is indeed the only subcluster whose “true” luminosity profile can be fitted by a β -model (the dotted line in Fig. 6f).

The failure of the β -model for the M87 and M49 subcluster luminosity profiles unfortunately deprives us of a simple deprojection (by Eq.(3)) and direct comparison with the gas density profiles. For such a comparison we have therefore to rely either on the number density profiles or again on the smoothed luminosity density profiles; in the latter case, however, it is correct only for the outer part, say $r \leq 70'$.

5.3. Comparison of galaxy number density and luminosity density

The profiles in Fig. 6 are shown with varying scale, making a comparison between number and luminosity density difficult. For the M87 subcluster, the number density and the smoothed luminosity density profiles (for both R and P) are plotted as deprojected, spatial densities in the same Fig. 7. As the profiles are centred on the brightest galaxy of the subcluster, there is the trend of the luminosity profile to be steeper than the number density profile in the inner part – even with smoothed luminosities. The

Table 2. Profile parameters and fit results for the number density of galaxies. The first column gives the galaxy on which the profile is centred. The second column shows how the galaxies were selected, either by the probability method (P) or by exclusion of rectangular regions (R) (see text). Column (3) gives the morphological type selected for the profile, “all” means that no type selection is applied. The binning (column 4) states how many galaxies are in each bin. Column (5) gives the outer cut-off radius. The fit parameters: central surface number density, core radius and slope parameter β are listed in columns (6), (7) and (8), respectively, with corresponding 1σ errors and χ^2 in column (9).

centre	selection	type	binning	radius (arcmin)	n_0 ($10^{-4}/\text{kpc}^2$)	r_c (arcmin)	β	reduced χ^2
M87	P	all	50	250	4.0 ± 0.5	83 ± 24	0.93 ± 0.13	0.85
M87	R	all	50	250	4.0 ± 0.3	65 ± 6	0.75 ± 0.03	0.44
M87	R	E+S0	10	250	0.43 ± 0.3	41 ± 65	0.79 ± 0.33	1.97
M87	P	dE+dS0	25	250	4.1 ± 0.6	84 ± 26	0.98 ± 0.15	0.80
M87	R	dE+dS0	25	250	3.5 ± 0.6	62 ± 24	0.79 ± 0.10	0.88
M87	R	Sp+Irr	25	250	0.25 ± 0.01	5000 ± 20	80 ± 0.5	0.28
M49	P	all	25	125	3.7 ± 0.2	28 ± 2	0.67 ± 0.02	0.81
M49	R	all	25	200	2.9 ± 0.6	55 ± 25	0.89 ± 0.17	0.86
M49	R	dE+dS0	25	200	2.7 ± 0.4	30 ± 5	0.74 ± 0.04	0.43
M49	R	Sp+Irr	16	200	0.45 ± 0.04	3100 ± 200	340 ± 40	0.62
M86	P	all	13	167	2400 ± 300	0.25 ± 0.03	0.91 ± 0.01	4.03

same trend holds for the other subclusters as well, which can be read from Tables 2 and 3: for the luminosity profiles β is larger while the core radius r_c is at the same time smaller by a factor of ≈ 2 than for the corresponding number density profiles. However, in the outer parts ($r > 70'$), number density and luminosity density are following nearly parallel curves. The difference is really only due to the central giant galaxies. There is no general luminosity segregation in the cluster. The galaxies, by number, are supposed to trace the gravitational potential of the cluster in a non-dissipative way. Their profile, if transformed in mass units, is indeed similar to the gravitational mass profile (see Sect. 6). In contrast, the central galaxies themselves (like most individual galaxies) underwent strong dissipation, leading to a steep luminosity profile – steeper than the luminosity profile of the surrounding cluster, as we have seen above (Fig. 6, right panels.). The deprojected “true” luminosity profile (from Fig. 6b) would of course look still much steeper than the smoothed one in Fig. 7.

The core radii of the number density fits, 480 and 380 kpc for P and R - profiles, respectively, are somewhat larger than the standard value for clusters of galaxies of 250 kpc (Bahcall 1975), while the core radii of the luminosity density fits are slightly smaller than this (160 and 150 kpc, respectively). All our core radii are significantly smaller than the value given by BTS87 with 650 kpc. One reason for this difference is certainly the fixed β -value in the fit of BTS87. β and r_c are strongly correlated, i.e. the χ^2 -ellipse of the fit is very elongated and the orientation is such that if one parameter is increased, the other increases as well. BTS87 used a large β ($\beta = 1$) compared

to ours, therefore they found a larger core radius. Another reason might be that in BTS87 the galaxies of the M86 subcluster were not excluded, and the centre of the radial bins was positioned between M87 and M86. Our central luminosity density, with $5.2 \times 10^{11} \mathcal{L}_{\odot,B}/\text{Mpc}^3$ for P -profiles and $5.6 \times 10^{11} \mathcal{L}_{\odot,B}/\text{Mpc}^3$ for R -profiles, is, however, quite similar to the one found by BTS87 ($5 \times 10^{11} \mathcal{L}_{\odot,B}/\text{Mpc}^3$).

In Figs. 2, 3 and 5 one sees a second concentration in the M87 subcluster around M60. Excluding the region around M60 results in an increase of β by 2-3 % for the number density and an increase by at most 10% for the luminosity density, leaving, however, the general trends shown in Fig. 7 unchanged. For all data given in the tables and shown in the figures, the M60 emission is included to make the optical results directly comparable to the X-ray results.

From Fig. 7 we note again the close agreement between R and P -profiles even for spatial densities.

5.4. Gas versus galaxies

We can compare the gas distribution with the galaxy distribution after deprojecting both in the way described in Sect. 5.1. The profile parameters and fit results for the X-ray profiles of the M87 and M49 subclusters are presented in Table 4. For the M86 subcluster no reliable X-ray profile could be determined. Note that the X-ray data were not smoothed here with $\sigma = 24'$ as they were for Fig. 1; the ROSAT All-Sky Survey resolution is better than $1'$. The deprojected, spatial gas density profile for the M87 subcluster is shown in Fig. 7 along with the galaxy number and *smoothed* luminosity densities discussed above. The

Table 3. Profile parameters and fit results for the luminosity distribution of galaxies. Columns (1)-(4) same as Table 2. Pc in column (2) denotes a P -profile with the observed luminosity profile of the central galaxy incorporated. The fit parameters: central surface luminosity density, core radius and slope parameter β are listed in columns (5), (6) and (7), respectively, with the corresponding 1σ errors and χ^2 in column (8).

centre	selection	type	radius (arcmin)	L_0 ($10^5 \mathcal{L}_{\odot,B}/\text{kpc}^2$)	r_c (arcmin)	β	reduced χ^2
M87	P	all	250	5.2 ± 1.4	28 ± 15	0.68 ± 0.07	0.54
M87	R	all	250	5.6 ± 0.1	25 ± 1	0.63 ± 0.01	0.42
M87	R	E+S0	250	5.4 ± 1.6	22 ± 9	0.81 ± 0.06	1.81
M87	R	dE+dS0	250	0.48 ± 0.12	26 ± 14	0.65 ± 0.07	0.53
M49	P	all	125	6.7 ± 1.3	29 ± 1	0.92 ± 0.01	0.21
M49	R	all	200	5.3 ± 0.3	57 ± 2	1.31 ± 0.02	0.71
M86	P	all	100	4.5 ± 0.8	56 ± 17	2.6 ± 0.8	0.82
M86	R	all	66	5.8 ± 0.1	≈ 1000	≈ 600	-
M86	Pc	all	100	5.3 ± 1.5	19 ± 6	1.2 ± 0.1	0.56

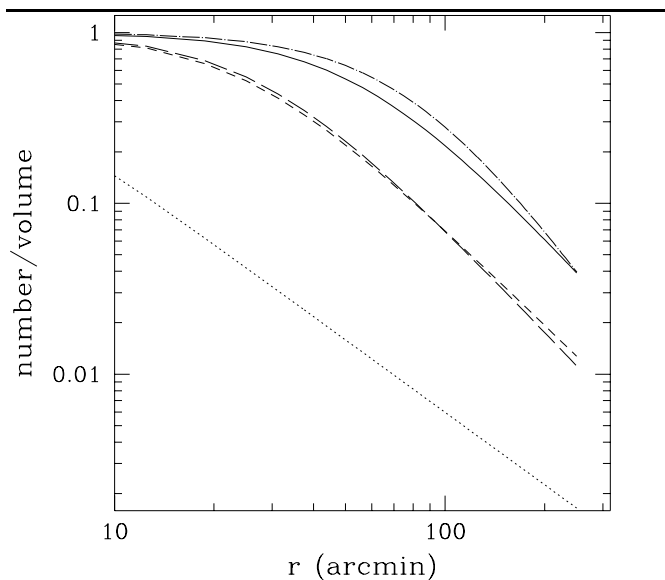


Fig. 7. Deprojected (spatial) density profiles for the M87 subcluster. All profiles are normalized to a central value of 1. The two upper lines show the number density of galaxies (dot-dashed line: P -profile, solid line: R -profile). The two lines in the centre show the luminosity density (long dashed line: P -profile, short dashed line: R -profile). The lower straight line (dotted) is the 3D gas density which is much steeper in the central part than the galaxy distribution because of a very small core radius.

situation for the M49 subcluster is very similar (see also Fig. 8).

Clearly, in the central part (inside 50 to 70') the gas density falls off much more steeply than either optical profile. Due to the normalization of $\rho_0 = 1$, this is seen by the fact that the gas profile lies much below the optical profiles. The gas profile has a very small core radius (2.7 or 16 kpc, see Table 4), which is an order of magnitude smaller than the core radius of the smoothed luminosity

distribution, although the core radius is by far not resolved in the ROSAT All-Sky Survey: an HRI observation yields a core radius of $10''$ (1 kpc). The artificial flattening due to the Survey point spread function does of course not affect the X-ray surface profile shown here.

Is the gas profile also steeper than the “true” luminosity profile in the inner part, i.e. the luminosity profile of the central galaxy M87 itself? (Note that only the smoothed 3D luminosity profile is shown in Fig. 7.) The answer, also for M49, is no. The profiles of the central giant galaxies are steeper than the gas density profiles. How can we know without deprojecting the galaxy profiles? Instead of doing this, which is non-trivial without β -model fits, one can invert the problem and treat the spatial gas density as a spatial galaxy density and project it back by putting the X-ray β -model parameters from Table 4 into Eq.(1), and then compare this with the actual, observed galaxy profiles. A steeper slope in projection means also a steeper slope in 3D. The projected gas density slopes, in the inner part, turn out to be somewhat steeper than the projected galaxy density profiles in Fig. 6b (M87) and 6d (M49). But the luminosity profiles of M87 and M49 (even in projection, the dash-dot lines in those figures) are still very much steeper than the projected gas densities

This is plausible. As mentioned before, while the galaxy number density (and the smoothed luminosity density as well) essentially traces the gravitational potential of the cluster, the X-ray gas will have suffered a certain (modest) amount of dissipation, thereby steepening the gas profile. The principal agent of dissipation here is the cooling flow. The X-ray component of M87 is indeed known to show a cooling flow with a mass accretion rate of about $10 \mathcal{M}_{\odot}/\text{yr}$ within a cooling flow radius of 100 kpc (Stewart et al. 1984; Nulsen & Böhringer 1995). M49 is suspected to have a cooling flow as well (Irwin & Sarazin 1996). But again, the galaxies themselves must have suffered much stronger dissipation still (by rapid cooling in

Table 4. X-ray profile parameters and fit results. The first column gives the galaxy on which the profile is centred. Columns (2) and (3) give the name of the region and the corresponding angular selection. Column (4) gives the outer cut-off radius. The fit parameters: central surface brightness, core radius and slope parameter β are listed in columns (5), (6) and (7), respectively.

centre	region	sector (N over E)	outer radius (arcmin [Mpc])	S_0 (counts/arcmin ² /s)	r_c (arcmin)	β
M87	all	0° – 360°	250 [1.5]	0.21	2.7	0.47
M87	SW	180° – 270°	250 [1.5]	0.17	4.4	0.52
M87	N	0° – 45°	250 [1.5]	0.25	2.4	0.46
M87	S	135° – 225°	250 [1.5]	0.25	2.4	0.47
M49	all	0° – 360°	30 [0.17]	0.029	3.0	0.76
	0.51					

an early epoch) and therefore have much steeper profiles than the gas components.

In the outer parts (beyond 50 to 70', see Fig. 7) the effect is reversed. Here the gas profile is flatter than the galaxy density profiles.

5.5. The subclusters in comparison

Already from a glance at Fig. 5 (left panels) we have noted a systematic trend in the appearance of the three subclusters (Sect. 4), in the sense that the poorer (less populous) a subcluster the more compact it appears. This can now be quantified by a comparison of the density profiles derived for the three subclusters.

In Fig. 8 the deprojected, normalized profiles of the subclusters are shown. Consider first the optical profiles. Up to a radius of about 10 - 15' the galaxy number density profiles are similar, but in the outer parts the fits confirm the tendency already noted by eye: the poorer the subcluster the steeper the radial profile. For clarity only the P -number density profiles are shown in Fig. 8, but the R -profiles, as well as the luminosity profiles show the same systematic trend.

To compare also the X-ray components of different subclusters, we tried to fit also the X-ray emission around M49 with a β -model, although there are clearly asymmetries in the X-ray halo (see Irwin & Sarazin 1996). The fit parameters are listed in Table 4. The core radius of the gas profile of the M49 subcluster, with 3'0 or 17 kpc, is almost as small as the one of M87, which is a signature that M49 has a cooling flow as well.

Furthermore, there is a faint extended X-ray component at larger radii around M49 with the following parameters: $S_0 = 3 \times 10^{-4}$ counts/ \square '/s, $r_c = 19'$, and $\beta=0.51$ for a fit between 30 and 125'. However, that far out the X-ray emission is already less than 30% of the background level, and we therefore neglect it for the following analysis.

The X-ray halo around M86 is even more asymmetric with its plume in the North-West (Rangarajan et al. 1995).

As the β -model assumes spherical symmetry we do not present a β -fit of the X-ray emission around M86 here.

The tendency seen in the optical – a steeper profile in poorer subclusters – is clearly reflected in the X-ray profiles of M87 and M49 (see Fig. 8). The luminosity profiles (R and P) and X-ray profiles of the M49 subcluster all have much larger β values than the corresponding profiles of the M87 subcluster, demonstrating its stronger concentration (see Tables 2, 3 and 4).

The compactness of the M86 subcluster is even more extreme (see Fig. 8), although the fit to the number density profile has to be regarded with some caution as the profile consists only of 4 bins. The luminosity P -profile had to be restricted to a radius of 100' because of a second bright galaxy at a distance of 150' from M86 (see Fig. 5d). Excluding that galaxy the fit gave plausible results (Table 3). For the luminosity R -profile, where the influence by the M87 subcluster was subtracted, the data could be used out to a radius of merely 66', resulting again in 4 bins. However, the compactness of the M86 subcluster is unlikely to be an artifact of the selection procedure but is probably real, as also some galaxies far away (out to 175') from M86 were selected to belong to it.

5.6. Distribution of the Hubble types

From the different distributions of the various Hubble types in Fig. 2 (number densities) and Fig. 3 (luminosities) one expects also different profiles. β -model parameters for different types in the M87 and M49 subclusters, for cases where such fitting was feasible at all, are given in Tables 2 and 3. The profiles for number densities of the different Hubble types around M87 are shown in Fig. 9. The trends, in accord with the morphology-density relation (Dressler 1980, also BTS87), are evident. While the profile for dwarf ellipticals is very similar to the all-type profile, the profile for elliptical plus S0s is somewhat steeper than both, because these types are most concentrated in the cluster. However, they are still much less concentrated than the gas in the inner part. Beyond $r \approx 50'$ this turns

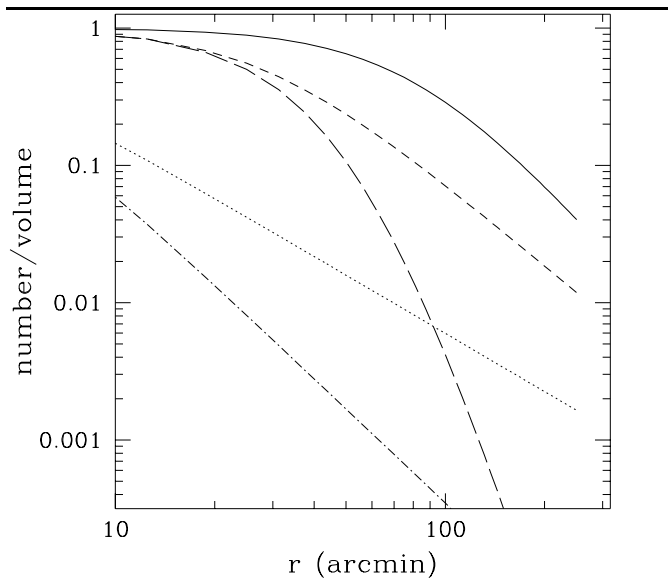


Fig. 8. Deprojected density profiles (P -profiles) of the various subclusters. All profiles are normalized to a central value of 1. The three upper lines show the number density of galaxies (solid line: M87 subcluster, short dashed line: M49 subcluster, long dashed line: M86 subcluster). The two lower lines show the 3D gas density derived from X-rays of the M87 subcluster (dotted line) and the M49 subcluster (dot-dashed line). Obviously, the poorer the subcluster the steeper is its profile, i.e. the more concentrated it is.

around and the gas component becomes shallower than these types. However, the gas component remains everywhere much steeper than spirals and irregulars, whose distribution is most dispersed. The luminosity profiles (not plotted) show the same trends.

5.7. Different regions around M87

A closer look at the X-ray emission around M87 (Figs. 1 and 2e) shows that it is not exactly spherically symmetric, but shows a bridge in the direction to M49, an elongation towards North, and a steep cut-off in the South-West (SW). To see the effect of these asymmetries, we have fitted X-ray profiles for different sectors of the M87 subcluster. The results are given in Table 4 and shown in Fig. 10. The region in the SW turns out to have a larger core radius and a larger β than the other sectors. The profiles of the other regions do not look very different from the overall profile.

For comparison, the same regions around M87 were extracted from the optical data. The corresponding optical profile parameters and fit results are listed in Table 5, and the profiles are again shown in Fig. 10. Obviously, the fits of the Northern and the Southern sector do not give significant results: the errors are exceedingly large due to the low number of galaxies. Only for the SW sector could an acceptable fit be achieved – again (as for the X-rays) with a large core radius and a large β . In Fig. 10 this

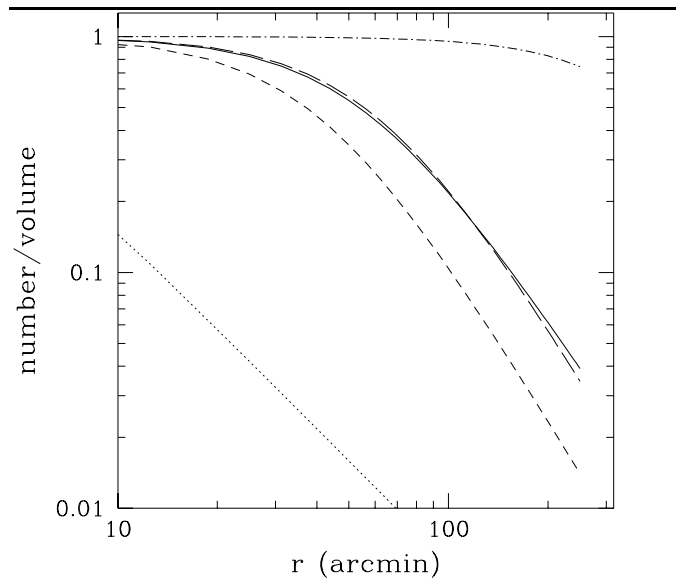


Fig. 9. Deprojected number density profiles (R -profiles) of the various morphological types of galaxies. The profiles are centred on M87 and are normalized to a central density of 1. The profile for dwarf elliptical galaxies (long dashed line) is very similar to the combined profile for all types (solid line). The profile for elliptical and S0 galaxies (short dashed line) is somewhat steeper, reflecting the compact distribution. On the other hand, the spiral and irregular galaxies (dot-dashed line) show a very flat profile. For comparison also the 3D gas density of the M87 subcluster is shown (dotted line).

shows up by a SW profile which is slightly steeper than the overall profile at large radii (more pronounced in the luminosity profile). This is the steep drop in density to the SW visible in Figs. 2a and 2e.

6. Mass profiles and mass-to-light ratios

From the galaxy luminosity densities we can easily construct radial mass density and integrated mass profiles by assigning every galaxy a mass-to-light ratio. For simplicity, and because we are mainly interested in the overall trends, we have adopted a constant mass-to-light ratio of 20 for every galaxy type. This number is of course arbitrary but seems realistic as an average (e.g. Binney & Tremaine 1987). Although there are hints that the mass-to-light ratio varies with the Hubble type (e.g., Burstein et al. 1995; Gavazzi et al. 1996), it should be emphasized that the mass determinations involved there refer to the integrated galaxy mass out to a given radius. The *total* masses of galaxies, which we would need here, are essentially unknown. It seems therefore safest at present to assume a constant mass-to-light ratio. Nevertheless, we should keep in mind that this simplifying assumption might introduce an additional uncertainty in the galaxy mass profiles because of the morphological segregation.

Table 5. Profile parameters and fit results for different regions around M87. All numbers listed are for R -profiles with an outer cutoff radius of $250'$. Column (1) indicates whether the projected number density or the projected luminosity density was fitted. Columns (2) and (3) give the name of the region and the corresponding angular selection. The binning (Column 4) is the number of galaxies per bin for the number densities and the constant bin size of $25'$ for the luminosity densities. Column (5) is the central projected number density and column (6) the central projected luminosity density. The core radius and β are listed in columns (7) and (8). In column (9) the reduced χ^2 is given.

density	region	sector (N over E)	binning	n_0 ($10^{-4}/\text{kpc}^2$)	L_0 ($10^5 \mathcal{L}_{\odot,B}/\text{kpc}^2$)	r_c (arcmin)	β	reduced χ^2
number	all	$0^\circ - 360^\circ$	50	4.0 ± 0.3		65 ± 6	0.75 ± 0.03	0.44
luminosity	all	$0^\circ - 360^\circ$	const		5.6 ± 0.1	25 ± 1	0.63 ± 0.01	0.42
number	SW	$180^\circ - 270^\circ$	25	4.1 ± 0.9		110 ± 70	1.1 ± 0.4	0.27
luminosity	SW	$180^\circ - 270^\circ$	const		3.6 ± 0.6	120 ± 40	1.5 ± 0.4	2.0
number	N	$0^\circ - 45^\circ$	25	3.6 ± 1.7		95 ± 115	0.95 ± 0.57	0.37
luminosity	N	$0^\circ - 45^\circ$	const		3.1 ± 0.3	1100 ± 600	40 ± 40	2.5
number	S	$135^\circ - 225^\circ$	25	3.8 ± 1.5		47 ± 52	0.63 ± 0.16	1.5
luminosity	S	$135^\circ - 225^\circ$	const		8.3 ± 8.2	8.2 ± 12	0.62 ± 0.05	0.60

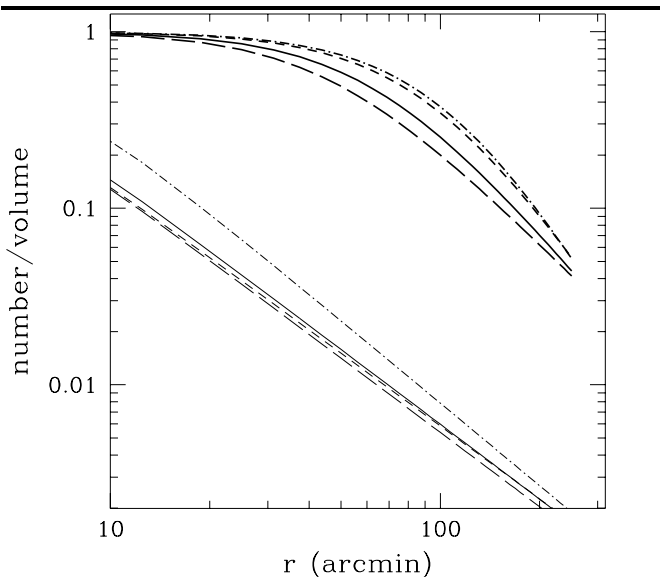


Fig. 10. Deprojected profiles of various regions (sectors) around M87. All profiles are normalized to a central density of 1. The four upper profiles (bold lines) show the number density of the galaxies (R -profiles) while the four lower profiles (thin lines) show the gas density: Total cluster (solid line), North (short dashed line), South (long dashed line) and South-West (dot-dashed line). For the definitions of the sectors see Tables 4 and 5.

The resulting profiles are shown in Fig. 11 (M87 subcluster) and Fig. 12 (M49 subcluster), where differential mass density profiles are given in the lower panels (b) and integrated (cumulative) mass profiles in the upper panels (a). A differentiation with respect to P and R -selected profiles shows little difference.

These mass profiles were constructed from the *smoothed* luminosity profiles, which strictly make sense only for the outer part, $r \geq 50 - 70'$ (remember Sect. 5.2). Further in

one would have to treat the luminous mass of the central giant galaxies M87 and M49, which is beyond our scope. The galaxy profiles shown in Figs. 11 and 12 therefore start only from $r = 60'$, corresponding to 0.35 Mpc with the adopted distance scale.

From the X-ray data we can derive mass profiles for the intra-cluster gas components of the two subclusters, which are also shown in Figs. 11 and 12. In the M87 subcluster the gas mass is dominating over the galaxy mass. At a radius of 1 Mpc the ratio M_{gal}/M_{gas} is 0.28 and 0.29 for the P - and the R -profile, respectively (see Table 6 for various mass ratios). These numbers are uncertain by $\approx 20\%$, which stems entirely from the uncertainty in the fitted luminosity profiles. The errors in the gas mass profiles are very small. The case is reversed for the M49 subcluster: here the gas mass is only a fraction of the mass in galaxies; at 750 kpc we have $M_{gal}/M_{gas} \approx 8$ (Table 6).

With the additional assumption of hydrostatic equilibrium we can use the X-ray gas as tracer of the total, gravitating mass profiles of the subclusters and derive these quantities by simply plugging our β -models with the parameters given in Table 4 into the well-known formula

$$M_{tot}(r) = \frac{-kr}{\mu m_p G} T \left(\frac{d \ln \rho}{d \ln r} + \frac{d \ln T}{d \ln r} \right), \quad (4)$$

where ρ and T are the density and the temperature of the intra-cluster gas, and r , k , μ , m_p , and G are the radius, the Boltzmann constant, the molecular weight, the proton mass, and the gravitational constant, respectively.

In Fig. 11 we show an integrated mass profile of the M87 subcluster (bold solid line) assuming an isothermal cluster of 2.7 keV. According to Böhringer et al. (1994), this temperature is acceptable for the radius range considered here (the cooling flow region is not included in this analysis). We show also a mass profile for a constant temperature gradient taken from the ROSAT data, which

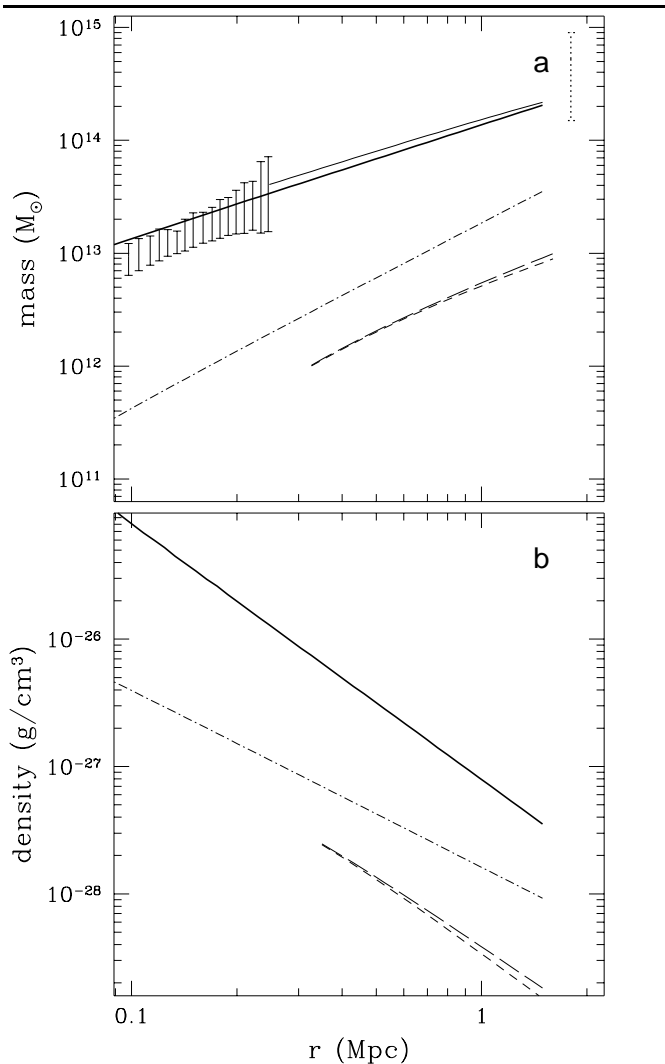


Fig. 11. Integrated mass (a) and differential mass density (b) profiles around M87. Shown are the gas mass (dash-dotted lines), the galaxy mass from a P -profile (short dashed line) and a R -profile (long dashed line), as well as the total (gravitating) mass assuming isothermal cluster gas (bold solid line). In panel (a) the thin solid line gives the integrated mass when a temperature gradient is assumed (see text). The solid error bars are from Nulsen & Böhringer (1995), and the dotted error bar indicates the total mass of the M87 subcluster estimated by Böhringer et al. (1994).

is a good approximation only for $r > 240$ kpc (the thin solid line). This temperature gradient is roughly in agreement with ASCA results of observations in North-West direction of M87 (Matsumoto 1998; Ohashi et al. 1998). Obviously, both profiles are very similar. We can compare these profiles with other X-ray derived masses (see Fig. 11a): the estimate at a large radius by Böhringer et al. (1994), also from the ROSAT All-Sky Survey data, and the detailed mass estimate by Nulsen & Böhringer (1995) derived from a deep pointed ROSAT/PSPC observation with 30000sec. Within the errors, both mass estimates

agree with our total mass profile. The error bars give an idea of the uncertainty in the total mass derived in this work. The largest uncertainty, with 30%, is probably in the temperature (Böhringer et al. 1994), so that we estimate an uncertainty in the total mass of 30-50%. Because of this large error, all results from this mass analysis must be taken with caution, showing tendencies rather than exact values. The masses for two different radii are listed in Table 6.

The total, gravitating mass is overwhelmingly larger than either the gas or galaxy mass, which is of course due to the presence of dark matter. The total mass profile is also slightly flatter than the gas mass profile in the M87 subcluster (see Fig. 11a). Within 400 kpc the gas mass accounts for 8% of the total mass, at 1 Mpc this fraction becomes 14% (Table 6), i.e. the gas-to-total mass ratio is increasing outwards, which is obvious from Fig. 11. Due to the large uncertainty in the total mass the increase between these two radii is not very significant. But when compared to the ratio at 100 kpc (3%) there is certainly a trend visible. The galaxy-to-total mass ratio, on the other hand, is only slightly increasing with radius: at 400 kpc, $M_{galaxies}/M_{tot} = 3\%$, while at 1 Mpc, $M_{galaxies}/M_{tot} = 4\%$.

The total mass profile of the M49 subcluster (Fig. 12) was calculated on the assumption of an isothermal gas with temperature 1.4 keV. This temperature was found by Irwin & Sarazin (1996) in the region around M49 (excluding the central part of M49).

Figure 12a shows also a comparison with other X-ray derived masses. The mass estimate by Böhringer et al. (1994) was again derived from the ROSAT All-Sky Survey data and is consistent with our estimate for the total mass (the dotted error bar). A mass estimate by Irwin & Sarazin (1996) based on ROSAT/PSPC and HRI pointed observations, after a scaling to the distance adopted here, disagrees with our mass profile by a factor of three (the data point with a solid error bar). We have no explanation for this discrepancy.

Compared to the M87 subcluster, the total mass profile of the M49 subcluster is systematically shifted to smaller values (see also Table 6). To compare the total, overall masses of the two subclusters, one has to take into account the fact that the M87 subcluster is more extended than the M49 subcluster. If one assumes a radius of 1.5 Mpc for the M87 subcluster and 0.75 Mpc for the M49 subcluster, one finds masses of $M_{tot,M87} = 2.1 \times 10^{14} \mathcal{M}_{\odot}$ and $M_{tot,M49} = 8.7 \times 10^{13} \mathcal{M}_{\odot}$, rendering the M87 subcluster about 2.4 times more massive than the M49 subcluster.

As noted above, the gas mass of the M49 subcluster is rather small, and even smaller than the galaxy mass. The gas mass profile in the M49 subcluster is also somewhat flatter than in the M87 subcluster (Fig. 12a), which comes from a rather steep density gradient (see Fig. 12b; note the different radius scale when comparing between Fig. 11 and Fig. 12). The gas mass in the M49 subcluster is always

Table 6. Masses of the subclusters centred on M87, M49 and M86 (integrated values). Galaxy masses are based on P -profiles with a constant $\mathcal{M}_\odot/\mathcal{L}_{\odot,B}$ of 20. The total masses of the M87 and M49 subclusters were calculated on the assumption of an isothermal gas. The total mass of the M86 subcluster is taken from Böhringer et al. (1994). The 1σ error for the galaxy masses is $\approx 20\%$, that for the total masses is 30-50% (except for M86).

	M87		M49		M86
	($r=400\text{kpc}$)	($r=1\text{Mpc}$)	($r=400\text{kpc}$)	($r=750\text{kpc}$)	($r=240\text{kpc}$)
$M_{tot}[10^{13}\mathcal{M}_\odot]$	5.5	14	4.7	8.7	1 – 3
$M_{gas}[10^{13}\mathcal{M}_\odot]$	0.42	1.9	0.026	0.044	-
$M_{gal}[10^{13}\mathcal{M}_\odot]$	0.14	0.51	0.17	0.34	0.06
M_{gas}/M_{tot}	8%	14%	0.6%	0.5%	-
M_{gal}/M_{tot}	3%	4%	4%	4%	2 – 6%
M_{gal}/M_{gas}	0.34	0.28	6.6	7.7	-
$M/L[\mathcal{M}_\odot/\mathcal{L}_{\odot,B}]$	≈ 500	≈ 500	≈ 500	≈ 600	300 – 1000

less than 1% of the total mass, which is much less than in the M87 subcluster (8 - 14%) and in other clusters. In contrast, the galaxy-to-total mass fraction is similar to the M87 subcluster (around 4%, see Table 6).

The galaxy masses are slightly different here for the P and the R -profiles. This difference is an indication of how large the errors are, which is hard to quantify otherwise. The difference in the integrated galaxy masses ($P - R$)/ P is at maximum 36%.

For comparison, a mass estimate for the M86 subcluster, taken from Böhringer et al. (1994) is also listed in Table 6. The total masses and galaxy masses are of course smaller than for the other two subclusters, but the ratio is very similar.

From the total mass profile and the (galaxy) luminosity profile we can calculate how the mass-to-light ratio changes with radius. This is shown in Fig. 13. Global mass-to-light ratios for the three subclusters are also given in Table 6. For the luminosities, P -profiles were used. We had again to restrict the fitted luminosity profiles of the M87 and M49 subclusters to $r > 350$ kpc, to avoid M87 and M49 themselves. Note that these M/L profiles are differential, i.e. are based on the 3D density profiles shown in Figs. 11b and 12b. Note also that this is independent of the mass-to-light ratios of single galaxies; here we deal essentially with the dark matter *between* the galaxies.

From Fig. 13a we can see that the mass-to-light ratio of the M87 subcluster is around $500 \mathcal{M}_\odot/\mathcal{L}_{\odot,B}$ with a tendency to decrease with radius. The ratio for the M49 subcluster is again around 500, but follows the inverse trend with radius: between 350 and 750 kpc it increases from 400 to 600 $\mathcal{M}_\odot/\mathcal{L}_{\odot,B}$. The mass-to-light ratio of the M86 subcluster is shown as large error bar, which is from the mass error bar given by Böhringer et al. (1994). The error in the mass-to-light ratio is dominated by the uncertainty in the mass (30-50%).

For comparison we show also, in Fig. 13b, the mass-to-light ratio projected onto the plane of the sky, i.e. calculated from the observed luminosity, and the projected

mass profiles. This way of presenting the ratio has two advantages. (1) The optical data can be used directly without fitting them with a model, so that we can use also the inner parts of the luminosity profiles, i.e. the ones with the correct central galaxy profile. (2) It is a quantity which can in principle be derived directly from observations, e.g. by a weak lensing analysis. However, the disadvantage is that we have to extrapolate the X-ray profiles to quite large radii in order to include all the mass. For the M87 subcluster, an extrapolation radius of 5 Mpc was necessary, while for the M49 subcluster a radius of 1.5 Mpc was found sufficient.

7. Summary and Discussion

The Virgo cluster, as the nearest cluster of galaxies, is ideally suited for a detailed comparison of the distribution of two components – intra-cluster gas and galaxies. For this purpose we have used the X-ray data from the ROSAT All-Sky Survey and the optical information from the VCC. Following the morphological studies of Binggeli et al. (1987, 1993) for galaxies, and Böhringer et al. (1994) for the X-ray gas, we have made first a qualitative, global comparison, and then concentrated on the three major subclusters of Virgo centred on M87, M49, and M86. For both components we have fitted the observed subcluster profiles with isothermal β -models, which allows easy de-projection to three-dimensional densities.

Apart from the new comparison with the distribution of the X-ray gas, as well as the construction of mass density and mass-to-light ratio profiles which can be inferred from the X-ray gas, we have extended the analysis by BTS87 in four respects: (1) While BTS87 used a constant exponent of -1 for the projected galaxy density (corresponding to a $\beta = 1$), we have left this parameter free for the fitting and – as can be seen in the tables – it indeed varies considerably. (2) We have developed a new technique (probability method P) for separating, i.e. decomposing the subclusters, based on both spatial and velocity

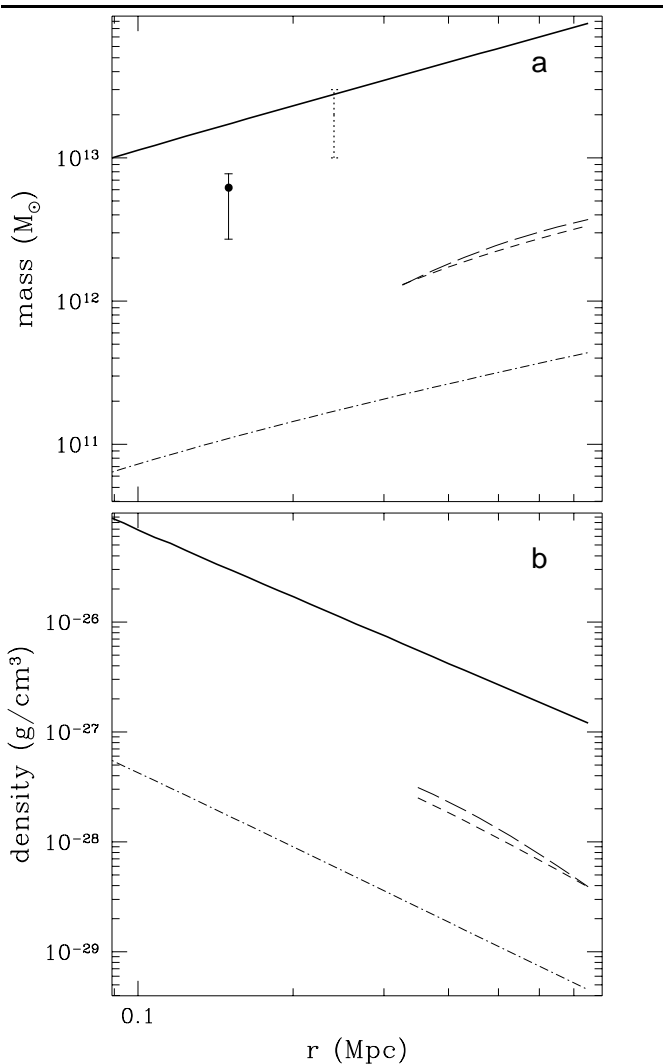


Fig. 12. Integrated mass (a) and differential mass density (b) profiles around M49. Symbols are the same as in Fig. 11. The solid error bar and data point in panel (a) shows the outermost mass estimate by Irwin & Sarazin (1996). The dotted error bar indicates the total mass given in Böhringer et al. (1994).

information. (3) We have determined radial profiles not only around M87, but also for the M49 and M86 subclusters. (4) We have explored also profiles in different sectors around M87.

The comparison of the X-ray and optical density profiles of the Virgo subclusters has led to the following results:

- The X-ray profile is steeper than the optical profile in the central part ($r < 70'$) but with a slight inverse trend at larger radii – for both the M87 and M49 subclusters. This is reflected in the much smaller X-ray core radii and the smaller X-ray β -values than the corresponding optical values. The reasons for the steep X-ray profiles in the central parts are probably the cooling flows in M87 and M49.

A comparison with a model of isothermal gas in hydrostatic equilibrium in a cluster where the dark matter is distributed with a NFW profile (Navarro et al. 1995) shows that the distributions of gas and dark matter have the same slope at radii larger than the core radius, while the gas distribution is flatter in the central part (Navarro et al. 1996). Obviously, the galaxies are not distributed like dark matter, but have a much flatter profile in the centre, even flatter than the gas distribution (however, this excludes the central galaxy itself whose luminosity profile is much steeper than the gas profile, and whose *mass* profile may indeed be similar to the gas profile, cf. Sect. 5.4). This effect can also be seen from the mass-to-light ratio profile which is not constant but shows a tendency of increasing mass for small radii. The same effect is reported by Carlberg et al. (1997) who also found an increasing mass-to-light ratio in the centre from their sample of 14 clusters. This effect cannot be an artifact of the total-mass determination because different methods were used. Carlberg et al. applied a virial approach for the determination of the total mass, while our total masses are based on X-ray observations.

- The more massive the subcluster the less compact is its structure – both in optical and in X-rays, i.e. poorer subclusters have a steeper radial profile. This behaviour is in agreement with the results of N-body simulations by Navarro et al. (1997) who also found steeper profiles for low-mass haloes than for high-mass haloes. The same systematic effect is well-known to hold also for normal elliptical galaxies (Kormendy 1977, 1985), i.e. low-luminosity ellipticals (like M32, but unlike “dwarf” ellipticals) appear much more compact than giant ellipticals. However, it is not clear why dissipation-less (sub)clusters and dissipational galaxies have so much in common, physically.

- Different Hubble types show different slopes in the subcluster profiles. We confirm the results by BTS87 that early-type galaxies are much more strongly clustered than late-type galaxies, reflecting of course the well-known morphology-density relation (Dressler 1980).

- There is a region South-West of M87 which shows a steeper gradient than the rest of the M87 subcluster – both in the optical and in X-rays. Steep gradients in the X-ray emission can be caused by shock waves emerging after the collision and merging of subclusters (Schindler & Müller 1993; Kulp & Schindler 1998). However, in such cases one finds usually a bulge or elongation of the collisionless particles in this direction, i.e. contrary to what is found in the galaxy distribution here. One can find steep gradients in the same directions only for non-central collisions where everything is twisted so that at a certain radius the bulge of the galaxy distribution and the shocks in the gas have an offset of 90° . In this case, however, one would expect to see other twists in the gas distribution. Therefore, the shock scenario is not a viable explanation here. Shortly before the collision the gas and the galaxy distributions have the same orientation, but this is also an unlikely sce-

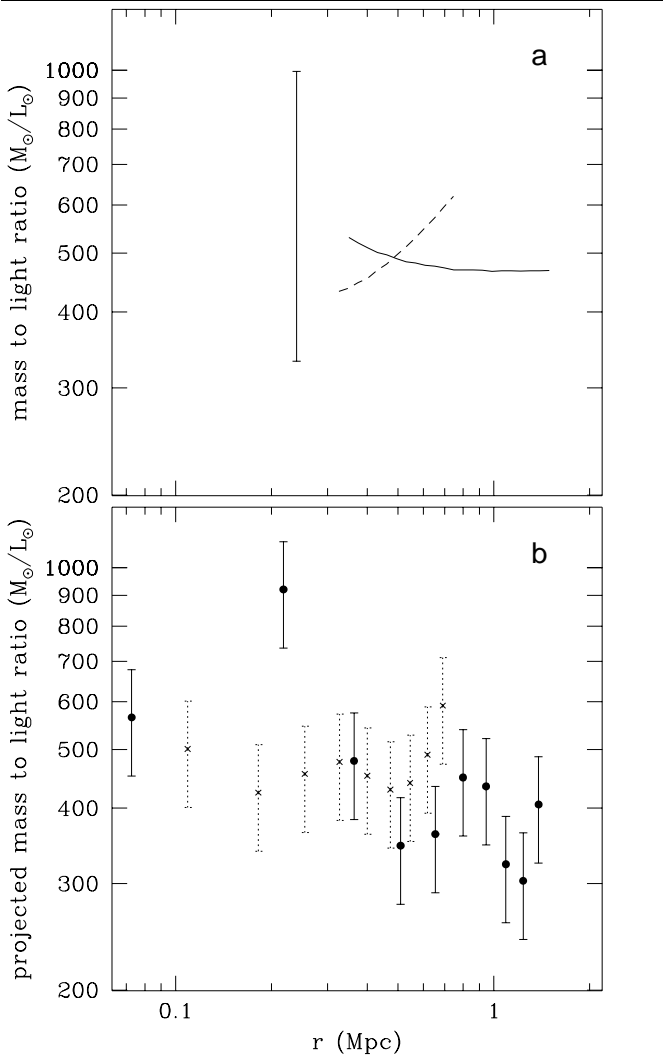


Fig. 13. a) 3D mass-to-light ratio profile for the M87 subcluster (solid line) and the M49 subcluster (dashed line). The range of the mass-to-light ratio for the M86 subcluster is shown as an error bar. b) 2D mass-to-light ratio (i.e. projected onto the plane of the sky) for the M87 subcluster (filled circles and solid error bars) and the M49 subcluster (crosses and dotted error bars). The errors plotted are only the errors in the galaxy luminosity profiles. The total uncertainties of all mass-to-light ratios (except for the M86 subcluster) are 30-50%.

nario for the subcluster M87, because there are no other indications (like, e.g., two very close concentrations, much closer than M87 to M86) of a forthcoming merger in the near future. It is possible though that a merger occurred a long time ago, at least 3 Gigayears ago, and what one sees is still a slight elongation in the direction of the original collision axis (which in this case would be SE-NW). From simulations one finds that this small elongation has the same direction for both components and remains stable for several Gigayears if there is no other event disturbing it. The reason why there is no steep slope on the other side of the assumed former collision axis (i.e. in the NE), might

simply be due to an infall or passage of a small group on this side destroying the symmetry.

– Differential and integrated profiles of the galaxy mass, gas mass, and total gravitating mass density are presented for both the M87 subcluster and the M49 subcluster. For the galaxy mass density we have excluded the central $60' = 0.35$ Mpc, because for that innermost region one would have to consider the radial profile of the central galaxy (i.e. M87 or M49) itself. The gas mass fraction in M87, with 8% and 14% at 400 kpc and 1 Mpc, respectively, is slightly on the low side for clusters, but is still in the normal range, cf. e.g. Böhringer (1994, 5 clusters: 12-45%); White & Fabian (1995, 19 clusters: 10-22%); Buote & Canizares (1996, 5 clusters: 8-22%); Briel et al. (1992, Coma: $30 \pm 14\%$); White et al. (1994, A478: 28%); Elbaz et al. (1995, A2163: $\approx 30\%$); Mohr et al. (1996, A576: 8%); Feretti et al. (1997, A2319: 20-35%); Neumann & Böhringer (1997, Cl0016+16: 14-32%); Schindler & Prieto (1997, A2634: $12^{+10}_{-5}\%$); Sarazin et al. (1998, A2029: $26 \pm 14\%$); Schindler et al. (1998, Cl0939+4713: 4-9%) (all scaled to $H_0 = 50 \text{ km s}^{-1} \text{ Mpc}^{-1}$). One finds the usual behaviour that the gas distribution is somewhat flatter than the distribution of the total mass, i.e. the gas distribution is more extended. This tendency was found in many clusters e.g. David et al. (1995, 10 clusters and groups); Allen et al. (1996, PKS0745-191); Böhringer et al. (1996, A3627); Sarazin & McNamara (1997, A2597); Schindler et al. (1997, RXJ1347.5-1145); Böhringer et al. (1998, A2390). The integrated gas mass is about 3 times the galaxy mass. This is about the same factor that was found in other clusters, e.g. Henry et al. (1993, A2256); Böhringer (1995, Perseus); Bardelli et al. (1996, A3558). A comparison of the gravitating mass of the M87 subcluster ($M_{tot,M87} = 2.1 \times 10^{14} M_\odot$) with the masses of other clusters shows that they are in general more massive than the M87 subcluster, e.g. the Coma and the Perseus cluster have almost a factor of ten more gravitating mass (Böhringer 1994). The galaxy mass density is getting flatter towards the centre, which is the reason why the mass-to-light ratio also tends to increase with decreasing radius (but again excluding M87 itself, i.e. for $r < 60'$). We find projected mass-to-light ratios between 300 and 500 $M_\odot/L_{\odot,B}$ at radii larger than 200 kpc which are relatively large mass-to-light ratios compared to the values of 90-250 $h_{50} M_\odot/L_\odot$ generally found in other clusters (cf. e.g. Hughes et al. 1989; Carlberg et al. 1996; Smail et al. 1997; Squires et al. 1997). But on the other hand some much higher values were found, e.g. 3300 $h_{50} M_\odot/L_\odot$ in AXJ2019+1127 (Hattori et al. 1997). In particular for the Virgo cluster a high value of 800 M_\odot/L_\odot (scaled to a distance of 20Mpc) was found by modeling velocity fields (Tully & Shaya 1998).

The mass distributions for the M49 subcluster are similar. The only quantity which differs substantially between the M87 and M49 subclusters, however, is the gas mass fraction. For the M49 subcluster we find a very small gas

mass fraction of less than 1% of the total mass. Even with the low total mass value of Irwin and Sarazin (1996), this fraction remains below 2%. Such a small gas fraction is very unusual for clusters. Even for galaxy groups the fraction is quite low, cf. e.g. Mulchaey et al. (1993, NGC2300: 2%); David et al. (1994, NGC5044: 6%); Pildis et al. (1995, 13 groups: maximum 2.8%; Neumann & Böhringer (1995, AWM7: 11-27%) (all scaled to $H_0 = 50 \text{ km s}^{-1} \text{ Mpc}^{-1}$). We have not found any plausible scenario which could explain this.

Acknowledgements. It is a pleasure to thank Doris Neumann for important discussions and Carlo Izzo for his most helpful EXSAS support. S.S. and H.B. thank the Verbundforschung, and B.B. the Swiss National Science Foundation for financial support.

References

- Allen S.W., Fabian A.C., Kneib J.-P., 1996, MNRAS 279, 615
- Bahcall N.A., 1975, AJ 98, 249
- Bardelli S., Zucca E., Malizia A., Zamorani G., Scaramella R., Vettolani G., 1996, A&A 305, 435
- Binggeli B., Sandage A., Tammann G.A., 1985, AJ 90, 1681
- Binggeli B., Tammann G.A., Sandage A., 1987, AJ 94, 251 (= BTS87)
- Binggeli B., Popescu C.C., Tammann G.A., 1993, A&AS 98, 275
- Binggeli B., 1998, in: Proceeding of the Ringberg workshop "M87", Röser H.-J., Meisenheimer K. (eds.), Springer, Berlin, in press
- Binney J., Tremaine S., 1987, Galactic Dynamics, Princeton University Press, Princeton, p. 589ff.
- Böhringer H., 1994, in: Cosmological Aspects of X-ray Clusters of Galaxies, Seitter, W.C. (ed.). NATO ASI Series C 441, Kluwer, Dordrecht, p. 123
- Böhringer H., 1995, in: Relativistic Astrophysics and Cosmology, Proceedings of the 17th Texas Symposium, Böhringer, H. et al. (eds.). The New York Academy of Sciences, New York, p. 67
- Böhringer H., Briel U.G., Schwarz R.A., Voges W., Hartner G., Trümper J., 1994, Nat. 368, 828
- Böhringer H., Neumann D.M., Schindler S., Kraan-Korteweg R.C., 1996, ApJ 467, 168
- Böhringer H., Tanaka Y., Mushotzky R.F., Ikebe Y., Hattori M., 1998, A&A 334, 789
- Briel U.G., Henry J.P., Schwarz R.A., Böhringer H., Ebeling H., Edge A.C., Hartner G., Schindler S., Trümper J., Voges W., 1991, A&A 246, L10
- Briel U.G., Henry J.P., Böhringer H., 1992, A&A 259, L31
- Buote D.A., Canizares C.R., 1996, ApJ 457, 565
- Burns J.O., Roettiger K., Pinkney J., Perley R., Owen F.N., Voges W., 1995, ApJ 446, 583
- Burstein D., Bender R., Faber S., Nolthenius R., 1995, Ap. Lett. & Comm. 31, 95
- Caon N., Capaccioli M., D'Onofrio M., 1993, MNRAS 265, 1013
- Carlberg R.G., Yee H.K.C., Ellingson E., Abraham R., Gravel P., Morris S., Pritchett C.J., 1996, ApJ 462, 32
- Carlberg R.G., Yee H.K.C., Ellingson E., 1997, ApJ 478, 462
- Cavaliere A., Fusco-Femiano R., 1976, A&A 49, 137
- David L.P., Jones C., Forman W., Daines S., 1994, ApJ 428, 544
- David L.P., Jones C., Forman W., 1995, ApJ 445, 578
- Dressler A., 1980, ApJ 236, 351
- Drinkwater M.J., Currie M.J., Young C.K., Hardy E., Yearsley J.M., 1996, MNRAS 279, 595
- Elbaz D., Arnaud M., Böhringer H., 1995, A&A 293, 337
- Federspiel M., Tammann G.A., Sandage A., 1998, ApJ 495, 115
- Feretti L., Giovannini G., Böhringer H., 1997, New Astron., 2, 501
- Fitchett M.J., 1988, in: The Minnesota Lectures on Clusters of Galaxies, ASP Conf. Ser. 5, Dickey, J.M. (ed.). Astronomical Society of the Pacific, San Francisco, p. 143
- Forman W., Schwarz J., Jones C., Liller W., Fabian A.C., 1979, ApJ 234, L27
- Gavazzi G., Pierini D., Boselli A., 1996, A&A 312, 397
- Girardi M., Escalera E., Fadda D., Giuricin G., Mardirossian F., Mezzetti M., 1997, ApJ 482, 41
- Hattori M., Ikebe Y., Asaoka I., Takeshima T., Böhringer H., Mihara T., Neumann D.M., Schindler S., Tsuru T., Tamura T., 1997, Nat. 388, 146
- Henry J.P., Briel U.G., Nulsen P.E.J., 1993, A&A 271, 413
- Hughes J.P., 1989, ApJ 337, 21
- Irwin J.A., Sarazin C.L., 1996, ApJ 471, 683
- Kormendy J., 1977, ApJ 218, 333
- Kormendy J., 1985, ApJ 295, 73
- Kulp K., Schindler S., 1998, in preparation
- McMillan S.L.W., Kowalski M.P., Ulmer M.P., 1989, ApJS 70, 723
- Matsumoto H., 1998, Ph.D thesis, in preparation
- Mohr J.J., Geller M.J., Fabricant D.G., Wegner G., Thorstensen J., Richstone D.O., 1996, ApJ 470, 724
- Morris P.W., Shanks T., 1998, MNRAS 298, 451
- Mulchaey J.S., Davis D.S., Mushotzky R.F., Burstein D., 1993, ApJ 404, L9
- Navarro J.F., Frenk C.S., White S.D.M., 1995, MNRAS 275, 720
- Navarro J.F., Frenk C.S., White S.D.M., 1996, ApJ 462, 563
- Navarro J.F., Frenk C.S., White S.D.M., 1997, ApJ 490, 493
- Neumann D.M., Böhringer H., 1995, A&A 301, 865
- Neumann D.M., Böhringer H., 1997, MNRAS 289, 123
- Nulsen P.E.J., Böhringer H., 1995, MNRAS 274, 1093

- Ohashi T., Kikuchi K., and the ASCA Virgo project team, 1997, in: Proceedings of the International Astronomical Union Symposium no. 188, The Hot Universe, Kyoto, p. 148
- Pildis R.A., Bregman J.N., Evrard A.E., 1995, ApJ 443, 514
- Rangarajan F.V.N., White D.A., Ebeling H., Fabian A.C., 1995, MNRAS 277, 1047
- Sarazin C.L., McNamara B.R., 1997, ApJ 480, 203
- Sarazin C.L., Wise M.W., Markevitch M.L., 1998, ApJ 498, 606
- Schindler S., Müller E., 1993, A&A 272, 137
- Schindler S., Prieto M.A., 1997, A&A 327, 37
- Schindler S., Hattori M., Neumann D.M., Böhringer H., 1997, A&A 317, 646
- Schindler S., Belloni P., Ikebe Y., Hattori M., Wambsganss J., Tanaka Y., 1998, A&A 338, 843
- Schröder A., 1995, Ph.D. thesis, Universität Basel.
- Smail I., Ellis R.S., Dressler A., Couch W.J., Oemler A.Jr., Sharples R.M., Butcher H., 1997, ApJ 479, 70
- Squires G., Neumann D.M., Kaiser N., Arnaud M., Babul A., Böhringer H., Fahlman G., Woods D., 1997, ApJ 482, 648
- Stewart G.C., Canizares C.R., Fabian A.C., Nulsen P.E.J., 1984, ApJ 278, 536
- Takano S., Awaki H., Koyama K., Kunieda H., Tawara Y., Yamauchi S., Makishima K., Ohashi T., 1989, Nat. 340, 289
- Tammann G.A., Federspiel M., 1996, in: The Extragalactic Distance Scale, Proceedings of the ST ScI May Symposium, Livio, M. et al. (eds.). Cambridge University Press, p. 137.
- Tonry J.L., Ajhar E.A., Luppino G.A., 1990, AJ 100, 1416
- Trümper J., 1993, Science 260, 1769
- Tully R.B., Shaya E.J., 1998, in: Proceedings of the MPA/ESO Cosmology Conference: Evolution of Large Scale Structure held in Garching, in press (astro-ph/9810298)
- Voges W., Boller T., Dennerl K., Englhauser J., Gruber R., Haberl F., Paul J., Pietsch W., Trümper J.E., Zimmermann H.U., 1996, in: Proceedings of the workshop Röntgenstrahlung from the universe, held in Würzburg, Germany, Zimmermann H.U., Trümper J.E., Yorke H. (eds.). MPE Report 263, p. 637
- West M.J., 1994, in: Clusters of Galaxies, Proceedings of the XIVth Moriond Astrophysics Meeting, Durrel, F. et al. (eds.). Editions Frontieres, Gif-sur-Yvette, p. 23
- White D.A., Fabian A.C., 1995, MNRAS 273, 72
- White D.A., Fabian A.C., Allen S.W., Edge A.C., Crawford C.S., Johnstone R.M., Stewart G.C., Voges W., 1994, MNRAS 269, 589
- White S.D.M., Briel U.G., Henry J.P., 1993, MNRAS 261, L8
- Zabludoff A.I., Zaritsky D., 1995, ApJ 447, L21

This article was processed by the author using Springer-Verlag \TeX A&A macro package 1992.